

THE STELLAR, GAS AND DYNAMICAL MASSES OF STAR-FORMING GALAXIES AT $Z \sim 2$ ¹

DAWN K. ERB², CHARLES C. STEIDEL³, ALICE E. SHAPLEY⁴,
MAX PETTINI⁵, NAVEEN A. REDDY³, KURT L. ADELBERGER⁶

Accepted for publication in ApJ

ABSTRACT

We present analysis of the near-infrared spectra of 114 rest-frame UV-selected star-forming galaxies at $z \sim 2$. By combining the H α spectra with photometric measurements from observed 0.3–8 μm , we assess the relationships between kinematics, dynamical masses, inferred gas fractions, and stellar masses and ages. The H α line widths give a mean velocity dispersion $\sigma = 101 \pm 5 \text{ km s}^{-1}$ and a mean dynamical mass $M_{\text{dyn}} = 6.9 \pm 0.6 \times 10^{10} M_{\odot}$ within a typical radius of $\sim 6 \text{ kpc}$, after excluding AGN. The average dynamical mass is ~ 2 times larger than the average stellar mass, and the two are correlated at the 2.5σ level and agree to within a factor of several for most objects, consistent with observational and systematic uncertainties. However, $\sim 15\%$ of the sample has $M_{\text{dyn}} \gg M_{\star}$. These objects are best fit by young stellar populations and tend to have high H α equivalent widths $W_{\text{H}\alpha} \gtrsim 200 \text{ \AA}$, suggesting that they are young starbursts with large gas masses. Rest-frame optical luminosity and velocity dispersion are correlated with 4σ significance; the correlation and its accompanying large scatter suggest that the processes which produce the correlation between luminosity and velocity dispersion in local galaxies are underway at $z \sim 2$. Fourteen of the 114 galaxies in the sample have spatially resolved and tilted H α emission lines indicative of velocity shear. It is not yet clear whether the shear indicates merging or rotation, but if the galaxies are rotating disks and follow relations between velocity dispersion and circular velocity similar to those seen in local galaxies, our observations underestimate the circular velocities by an average factor of ~ 2 and the sample has $\langle V_c \rangle \sim 190 \text{ km s}^{-1}$. Using the local empirical correlation between star formation rate per unit area and gas surface density, we estimate the mass of the gas associated with star formation, and find a mean gas fraction of $\sim 50\%$ and a strong decrease in gas fraction with increasing stellar mass. The masses of gas and stars combined are considerably better correlated with the dynamical masses than are the stellar masses alone, and agree to within a factor of three for 85% of the sample. The combination of kinematic measurements, estimates of gas masses, and stellar population properties suggest that the factor of ~ 500 range in stellar mass across the sample cannot be fully explained by intrinsic differences in the total masses of the galaxies, which vary by a factor of ~ 40 ; the remaining variation is due to the evolution of the stellar population and the conversion of gas into stars.

Subject headings: galaxies: evolution — galaxies: high redshift – galaxies: kinematics and dynamics

1. INTRODUCTION

A galaxy’s mass is one of its most fundamental properties. Both popular models of galaxy formation and recent observations suggest that mass is an important factor in determining when and how quickly galaxies form their stars; star formation in more massive galaxies is both expected and observed to start at earlier times (e.g. Davé et al. 2005; Heavens et al. 2004; Juneau et al. 2005). The redshift range $1.5 \lesssim z \lesssim 2.5$ has been shown to be particularly important both for the buildup of stellar mass and for accretion onto massive black

holes. A large fraction of the stellar mass in the universe today likely formed at $z > 1$ (Dickinson et al. 2003; Rudnick et al. 2003), and this redshift range also sees the peak of bright QSO activity (Fan et al. 2001; Di Matteo et al. 2003). Effective techniques now exist for the selection of galaxies at $z \sim 2$; these use the galaxies’ observed optical (Steidel et al. 2004) or near-infrared (Franx et al. 2003) colors, or a combination of the two (Daddi et al. 2004), and can be used to select both star-forming and passively evolving galaxies.

Even with large galaxy samples mass is difficult to measure, especially at high redshift. While galaxy formation models most naturally parameterize galaxies as a function of mass, observers can only determine mass through the measurement of luminosity or (preferably but with more difficulty) kinematic properties. Measurements of galaxy mass at high (and low) redshift take a variety of approaches. The most direct methods use kinematic tracers to measure the depth of a galaxy’s potential well. At relatively low redshifts, when rotation curves can be traced to large radii and galaxies’ mass distributions modeled, this technique yields relatively robust measurements, as shown by the good agreement between results derived from optical emission lines and 21 cm mapping of H I (e.g. Courteau 1997; Kobulnicky & Gebhardt

¹ Based on data obtained at the W.M. Keck Observatory, which is operated as a scientific partnership among the California Institute of Technology, the University of California, and NASA, and was made possible by the generous financial support of the W.M. Keck Foundation.

² Harvard-Smithsonian Center for Astrophysics, MS 20, 60 Garden St., Cambridge, MA 02138; derb@cfa.harvard.edu

³ California Institute of Technology, MS 105–24, Pasadena, CA 91125

⁴ Department of Astrophysical Sciences, Princeton University, Peyton Hall, Ivy Lane, Princeton, NJ 08544

⁵ Institute of Astronomy, Madingley Road, Cambridge CB3 0HA, UK

⁶ McKinsey and Company, 1420 Fifth Avenue, Suite 3100, Seattle, WA, 98101

2000). At high redshift the situation is more complicated. While spatially resolved “rotation curves” can sometimes be obtained using nebular emission lines in the near-IR (Pettini et al. 2001; Erb et al. 2003, 2004; Förster Schreiber et al. 2006), the limitations imposed by the seeing mean that they do not necessarily provide a unique kinematic model. A more robust measurement is the velocity dispersion, which can be measured for most high redshift galaxies and is less affected by the seeing. Velocity dispersions have been used to estimate the dynamical masses of relatively small samples of galaxies at $z \sim 2$ and $z \sim 3$; results typically range from $\sim 10^{10}$ to $\sim 10^{11} M_{\odot}$ (Pettini et al. 2001; Erb et al. 2003, 2004; van Dokkum et al. 2004; Swinbank et al. 2004). A model for the mass distribution is still required to turn a measurement of the velocity dispersion into a mass estimate, and this is a significant source of uncertainty in such dynamical masses.

Dynamical masses measured from velocity dispersions do not, of course, trace the full halo masses of high redshift galaxies; detectable nebular line emission is typically confined to sites of active star formation within a central region of a few kpc. Halo masses can be estimated less directly, however, through the galaxies’ clustering properties and the predicted clustering properties of halos as a function of mass. Adelberger et al. (2005b) find that the correlation lengths of the $z \sim 2$ rest-frame UV-selected galaxies on which this paper focuses correspond to halos with a typical mass of $\sim 10^{12} M_{\odot}$.

Estimations of stellar mass at high redshift are increasingly common, driven by wide-field IR detectors which allow large samples of rest-frame optical photometry, and by the Spitzer Space Telescope which enables detection of rest-frame near-IR light. Stellar masses of $z \sim 2$ –3 galaxies are determined through population synthesis models applied to such broadband photometry (e.g. Papovich et al. 2001; Shapley et al. 2001; Förster Schreiber et al. 2004; Shapley et al. 2005, among many others); the masses obtained range from $\sim 10^9$ to $\gtrsim 10^{11} M_{\odot}$. Such masses usually represent lower limits to the true stellar mass, however, since it is possible for the light from older populations of stars to be obscured by current star formation.

The most difficult component of a galaxy’s baryonic mass to measure at high redshift is its gas. For the most luminous, gas-rich, or gravitationally magnified examples, this can be estimated with millimeter observations (e.g. Baker et al. 2004; Greve et al. 2005), but for the typical $z \sim 2$ galaxy such observations are still out of reach. As the gas probably accounts for a significant fraction of the baryonic mass in young galaxies at high redshift, we have made use of the empirical correlation between star formation rate density and gas surface density to estimate the gas masses of the galaxies considered here.

This paper is one of several making use of a large sample of H α spectra of 114 $z \sim 2$ galaxies. In this work we discuss the galaxies’ kinematic properties and their stellar and dynamical masses, while Erb et al. (2006b) is devoted to star formation. This paper is organized as follows. We describe the selection of our sample, the observations, and our data reduction procedures in §2. In §3 we outline the modeling procedure by which we determine stellar masses and other stellar population param-

eters. §4 is devoted to the galaxies’ dynamical masses as derived from the H α line widths; we compare them with stellar masses in §4.1, and assess the relationship between velocity dispersion and rest-frame optical luminosity in §4.2. We compare the distributions of velocity dispersions of galaxies at $z \sim 2$ and $z \sim 3$ in §4.3. In §5 we examine galaxies with spatially resolved and tilted emission lines. §6 describes our estimates of gas masses from the local correlation between star formation rate and gas density per unit area, and comparisons of stellar, gas and dynamical masses. We summarize our conclusions and discuss our results in §7. Separately, we use the same sample of H α spectra to construct composite spectra according to stellar mass to show that there is a strong correlation between increasing oxygen abundance as measured by the [N II]/H α ratio and increasing stellar mass (Erb et al. 2006a). Galactic outflows in this sample are discussed by Steidel et al (2006, in preparation).

A cosmology with $H_0 = 70 \text{ km s}^{-1} \text{ Mpc}^{-1}$, $\Omega_m = 0.3$, and $\Omega_{\Lambda} = 0.7$ is assumed throughout. In such a cosmology, $1''$ at $z = 2.24$ (the mean redshift of the current sample) corresponds to 8.2 kpc, and at this redshift the universe is 2.9 Gyr old, or 21% of its present age. For calculations of stellar masses and star formation rates we use a Chabrier (2003) initial mass function (IMF), which results in stellar masses and SFRs 1.8 times smaller than would be obtained with a Salpeter (1955) IMF.

2. SAMPLE SELECTION, OBSERVATIONS AND DATA REDUCTION

The galaxies discussed herein are drawn from the rest-frame UV-selected $z \sim 2$ spectroscopic sample described by Steidel et al. (2004). The candidate galaxies were selected by their U_nGR colors (from deep optical images discussed by Steidel et al. 2004), with redshifts for most of the objects in the current sample then confirmed in the rest-frame UV using the LRIS-B spectrograph on the Keck I telescope. The total sample of 114 H α spectra consists of 75 new observations and 39 that have been published previously (Erb et al. 2003, 2004; Shapley et al. 2004). In total we attempted 132 galaxies with previously known redshifts, but 23 were not detected. We also attempted to observe 28 galaxies without previously known redshifts but which met the photometric selection criteria; only 5 of these yielded secure H α redshifts. Most of the undetected galaxies have $K > 21.5$, while most of those we detect have $K < 21.5$; we are less likely to detect H α emission for objects that are faint in K . This is not surprising, given the correlation between K magnitude and star formation rate recently found for the $z \sim 2$ sample by Reddy et al. (2005). This correlation is confirmed and discussed by Erb et al. (2006b)

The set of galaxies presented here is not necessarily representative of the UV-selected sample as a whole, because objects were chosen for near-IR spectroscopy for a wide variety of reasons. Criteria for selection included: 1) galaxies near the line of sight to a QSO, for studies of correlations between galaxies and metal systems seen in absorption in the QSO spectra (Adelberger et al. 2005a); 2) morphologies—elongated in most cases, with a few more compact objects for comparison; most of these have been previously discussed by Erb et al. 2004; 3) galaxies with red or bright near-IR colors or magnitudes, or oc-

asionally those whose photometry suggested an unusual spectral energy distribution (SED; 13 objects selected because they have $K < 20$ are discussed by Shapley et al. 2004); 4) galaxies that have excellent deep rest-frame UV spectra, or are bright in the rest-frame UV; 5) in order to confirm classification as AGN; or 6) members of close pairs with redshifts known to be favorable relative to night sky lines. The remaining objects are galaxies within $\sim 25''$ of our primary targets, which were placed along the slit and observed simultaneously with the primary targets. A significant number of galaxies meet more than one of these criteria. The sightline and secondary pair objects are therefore generally representative of the UV-selected sample as a whole, while the addition of the IR red or bright objects means that the total H α sample is somewhat biased toward more massive galaxies (see §3). We identify AGN as galaxies that show broad and/or high ionization emission lines in their rest-frame UV spectra, or as objects with broad H α lines or very high [N II]/H α ratios. The AGN fraction (5/114) is similar to the fraction found for the full spectroscopic sample in the GOODS-N field by Reddy et al. (2005), using direct detections in the 2-Ms *Chandra* Deep Field North images.

In order to assess the representativeness of the NIRSPEC sample, in Figure 1 we compare the colors and magnitudes of the galaxies in the NIRSPEC sample with that of all spectroscopically confirmed UV-selected galaxies in the same fields and redshift range. The top panels show \mathcal{R} vs. $G - \mathcal{R}$ (upper left) and $G - \mathcal{R}$ vs. $U_n - G$ (upper right). The shaded regions in the upper right panel show the selection criteria for, from top to bottom, the $z \sim 3$ C/D and MD galaxies (Steidel et al. 2003) and the $z \sim 2$ BX and BM galaxies (Steidel et al. 2004). Objects that fall outside the selection windows were either selected using earlier photometry or criteria extending slightly blueward in $U_n - G$. The lower panels show K_s vs. $\mathcal{R} - K_s$ at lower left, and K_s vs. $J - K_s$ at lower right. These comparisons show that the NIRSPEC sample spans nearly the full range in \mathcal{R} and K_s magnitudes and in $\mathcal{R} - K_s$ and $J - K_s$ colors. We have observed ~ 30 – 50% of the galaxies with NIRSPEC at the bright and red ends of the distributions, and $\sim 10\%$ at the faint and blue ends. Most objects selected by the BX/BM criteria have $G - \mathcal{R} < 0.5$, as do all but three galaxies in the NIRSPEC sample; the reddest and bluest galaxies in $G - \mathcal{R}$ are somewhat underrepresented.

For the purposes of comparisons with other surveys, we note that 10 of the 87 galaxies for which we have H α spectra and JK_s photometry have $J - K_s > 2.3$ (the selection criterion for the FIREs survey, Franx et al. 2003); this is similar to the $\sim 12\%$ of UV-selected galaxies which meet this criterion (Reddy et al. 2005). 18 of the 93 galaxies for which we have K magnitudes have $K_s < 20$, the selection criterion for the K20 survey (Cimatti et al. 2002); this is a higher fraction than is found in the full UV-selected sample ($\sim 10\%$), because we intentionally targeted many K -bright galaxies (Shapley et al. 2004). Four of the 10 galaxies with $J - K_s > 2.3$ also have $K_s < 20$.

2.1. Near-IR Spectra

All of the H α spectra (with the exceptions of CDFb-BN88, Q0201-B13, and SSA22a-MD41, which

were observed with the ISAAC spectrograph on the VLT and previously discussed by Erb et al. 2003) were obtained using the near-IR spectrograph NIRSPEC (McLean et al. 1998) on the Keck II telescope. Observing runs were in May 2002, May, July and September 2003, and June and September 2004. The conditions were generally photometric with good (~ 0.5 – $0.6''$) seeing, with the exceptions of the May 2003 and June 2004 runs which suffered from occasional clouds and seeing up to $\sim 1''$. H α falls in the K -band for the redshift range $2.0 \lesssim z \lesssim 2.6$, which includes the vast majority of the current sample; 6 of the 114 objects have $1.4 \lesssim z \lesssim 1.8$, and were observed in the H -band. We use the $0.76'' \times 42''$ slit, which, in NIRSPEC's low resolution mode, provides a resolution of $\sim 15 \text{ \AA}$ ($\sim 200 \text{ km s}^{-1}$; $R \simeq 1400$) in the K -band.

Our observing procedure is described by Erb et al. (2003). For a typical object, we use four 15 minute integrations, although the number of exposure varied from 2 to 6 for total integrations of 0.5 to 1.5 hours. We perform blind offsets from a nearby bright star, returning to the offset star between each integration on the science target to recenter and dither along the slit. In most cases we attempt to observe two galaxies with separation $< 25''$ simultaneously by placing them both on the slit; thus the position angle is set by the positions of the two galaxies.

The spectra were reduced using the standard procedures described by Erb et al. (2003). Uncertainties were accounted for via the creation of a two-dimensional frame of the statistical 1σ error appropriate to each pixel. The last step in the reduction was to extract one-dimensional spectra of each galaxy; this was done by summing the pixels containing a signal along the slit. The same aperture was then used to extract a variance spectrum from the square of the error image described above; the square root of this is a 1σ error spectrum, which was used to determine the uncertainties in the line fluxes and widths. Line centroids, fluxes and widths were measured by fitting a Gaussian profile to the line using the IRAF task *splot*, with the base fixed to the average value of the continuum (we do not detect significant continuum flux for most of the objects in the sample). The *splot* task provides 1σ statistical uncertainties for each of the fitted quantities, which are determined by a series of Monte Carlo simulations which perturb the spectrum according to the 1σ uncertainties determined from the error spectrum described above. The objects observed are listed in Table 1, and some representative examples of the spectra are shown in Figure 2. Others are presented by Erb et al. (2003) and Shapley et al. (2004).

2.2. Near-IR Imaging

J -band and K_s -band images were obtained with the Wide-field IR Camera (WIRC; Wilson et al. 2003) on the 5-m Palomar Hale telescope, which uses a Rockwell HgCdTe Hawaii-2 $2k \times 2k$ array, with a field of view of $8.5' \times 8.5'$ and spatial sampling of 0.249 arcseconds per pixel. Observations were conducted in June and October 2003 and April, May and August 2004. Some images were also taken in June 2004, courtesy of A. Blain and J. Bird. We used 120-second integrations (four 30-second coadds in K , one 120-second coadd in J), typically in a randomized $\sim 8''$ dither pattern of 27 exposures. Total exposure times and 3σ image depths in each field are

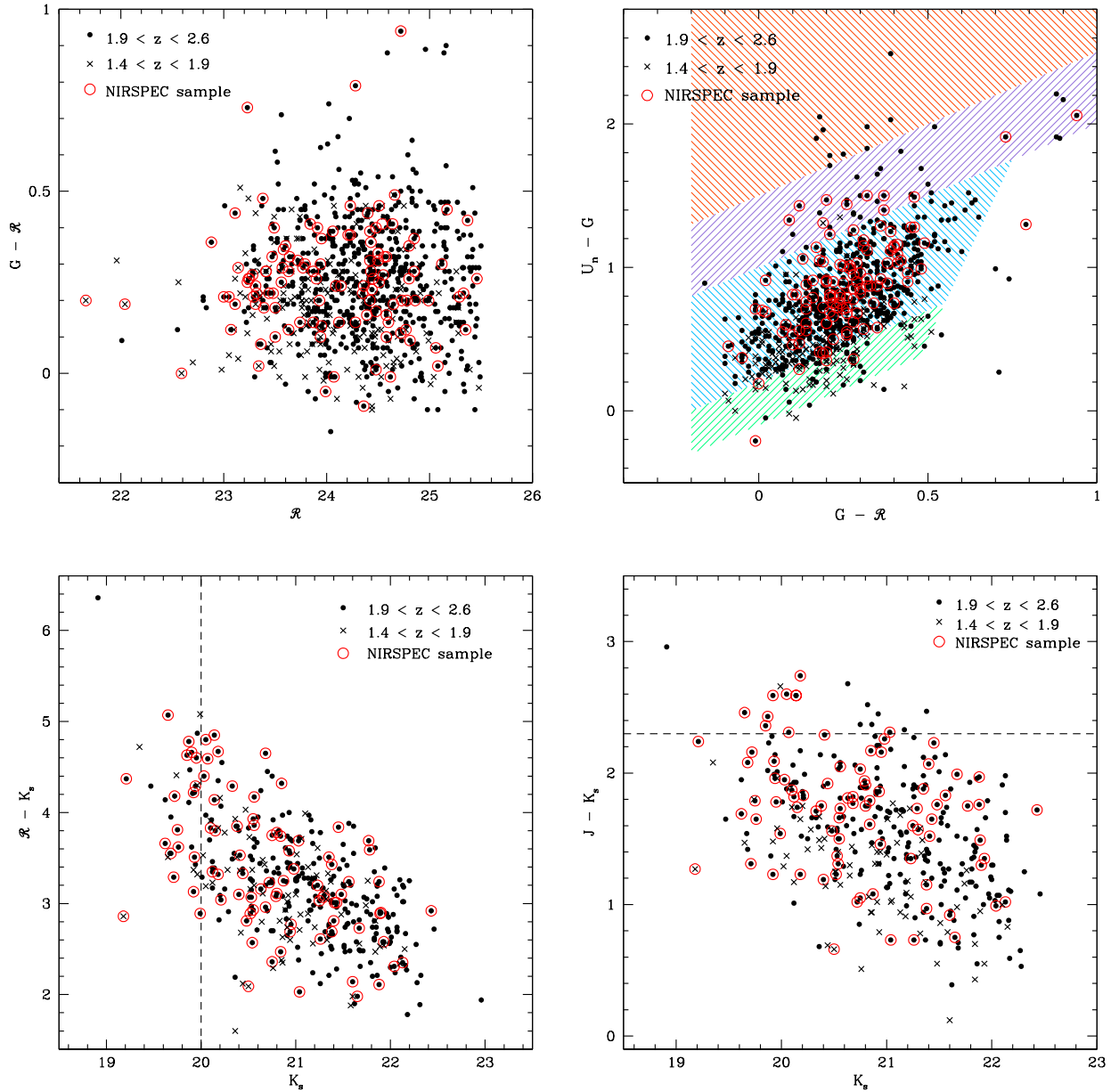


FIG. 1.— Photometric comparisons of the NIRSPEC sample with all spectroscopically confirmed U_nGR -selected galaxies in the same fields and redshift range. The top panels compare the rest-frame UV photometry: \mathcal{R} vs. $G - \mathcal{R}$ at upper left, and $G - \mathcal{R}$ vs. $U_n - G$ at upper right. From top to bottom, the shaded regions show selection criteria for the $z \sim 3$ LBGs (C/D and MD, Steidel et al. 2003) and for BX and BM galaxies (Steidel et al. 2004). Objects that fall outside the selection windows were either selected using earlier photometry or criteria extending slightly blueward in $U_n - G$. In the bottom panels we compare the near-IR photometry: K_s vs. $\mathcal{R} - K_s$ at lower left, and K_s vs. $J - K_s$ at lower right. The dashed lines show $K_s = 20$ and $J - K_s = 2.3$ in the left and right panels respectively. We include objects with $1.4 < z < 1.9$; 6 of the 114 objects in the NIRSPEC sample are in this redshift range.

given in Table 2.

Only those images with seeing as good as or better than our optical images (typically $\sim 1.2''$; $0.85''$ in the Q1700 field) were incorporated into the final mosaics. The images from each dither sequence were reduced, registered and stacked using IDL scripts customized for WIRC data by K. Bundy (private communication). The resulting images were then combined and registered to our optical images using IRAF tasks. Flux calibration was performed with reference to the 15–30 2MASS stars in each field. We have also used a 45 min image of Q2346-BX404 and Q2346-BX405 from the near-IR cam-

era NIRC (Matthews & Soifer 1994) on the Keck I telescope taken on 1 July 2004 (UT), courtesy of D. Kaplan and S. Kulkarni; this image was reduced similarly, and flux-calibrated by matching the magnitudes of objects in the field to their magnitudes in the calibrated Q2346 WIRC image.

Photometry was performed as described by Shapley et al. (2005). Briefly, galaxies were detected (i.e., found to consist of connecting pixels with flux at least three times the sky σ and area greater than the seeing disk) in the \mathcal{R} -band catalogs as described in detail by Steidel et al. (2003), with total

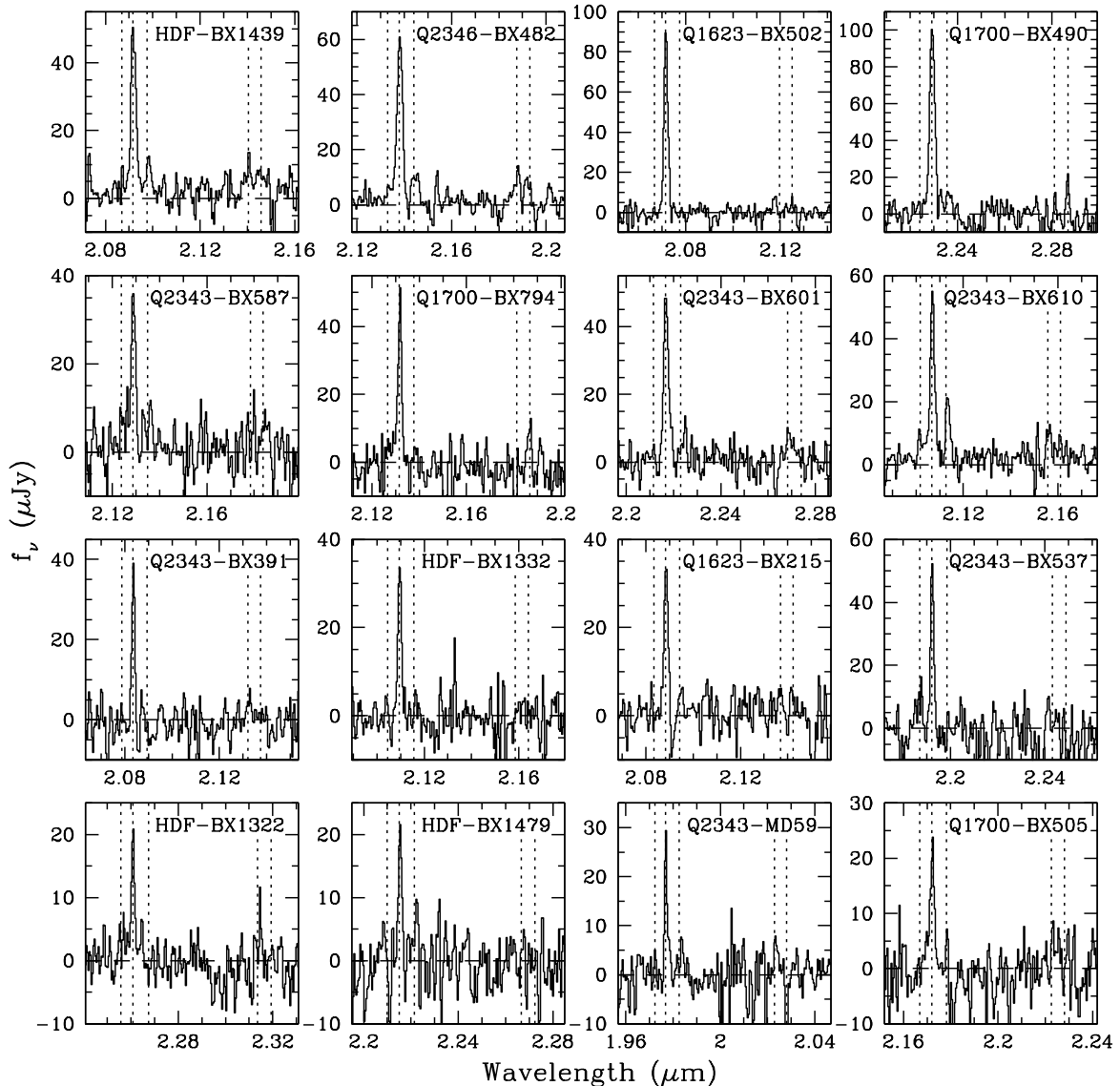


FIG. 2.— Representative examples of the $H\alpha$ spectra. Each row shows objects drawn from each quartile of $H\alpha$ flux: the top row contains galaxies drawn from the highest quartile in flux, the second row from the second highest quartile, the third row from the third highest quartile, and the bottom row from the lowest quartile. The dotted lines in each panel show, from left to right, the locations of $[N\ II]\lambda 6548$, $H\alpha$, $[N\ II]\lambda 6583$, $[S\ II]\lambda 6716$, and $[S\ II]\lambda 6732$.

\mathcal{R} magnitudes determined by increasing the isophotal detection aperture by a factor of two in area. $\mathcal{R} - K$ and $\mathcal{R} - J$ colors were determined by applying the \mathcal{R} -band detection isophotes to the J and K images; the J and K magnitudes were then determined from the total \mathcal{R} magnitudes and the $\mathcal{R} - K$ and $\mathcal{R} - J$ colors. We also applied the detection algorithm to the K -band images, and then applied the resulting isophotes to the J -band images. This procedure resulted in two sets of J and K magnitudes which typically differed by ~ 0.3 mag or less, comparable to the photometric uncertainties derived from the simulations described below; these differences arise because the \mathcal{R} -band total aperture may not include all of the K -band light, or vice versa. For the final J and K photometry, we adopted the more significant of the two magnitudes for each galaxy. The additional detection in K represent a change in method from that used by Shapley et al. (2005); this change, as well as a slight change in the photometric zeropoints from new flux calibrations, means that some magni-

tudes given here may be slightly different than those previously published (Shapley et al. 2004, 2005). We have also trimmed noisy, less well-exposed edge regions of the K -band images somewhat more than previous versions for cleaner detections in K , with the result that some objects with previously published magnitudes are no longer in the K -band sample. Photometric uncertainties were determined by adding a large number of fake galaxies of known magnitudes to the images, and detecting them in both \mathcal{R} and K bands to mimic our photometry of actual galaxies. This process is described in detail by Shapley et al. (2005). As noted in §4, the photometric apertures used here are approximately the same size as those used to determine dynamical masses from the $H\alpha$ spectroscopy.

2.3. Mid-IR Imaging

Two of our fields have been imaged by the Infrared Array Camera (IRAC) on the Spitzer Space Telescope. Images of the Q1700 field were obtained in Oc-

tober 2003 during the ‘‘In-Orbit Checkout’’, and have been previously discussed in detail (Barnby et al. 2004; Shapley et al. 2005). We also make use of the fully reduced IRAC mosaics of the GOODS-N field, which were made public in the first data release of the GOODS Legacy project (M. Dickinson, PI). These images are described in more detail by Reddy et al. (2005). For both fields we use the photometric procedure described by Shapley et al. (2005).

3. MODEL SEDS AND STELLAR MASSES

3.1. Modeling procedure

We determine best-fit model SEDs and stellar population parameters for the 93 galaxies for which we have K -band magnitudes. Most of these (87) also have J -band magnitudes, and 35 (in the GOODS-N and Q1700 fields) have been observed with the IRAC camera on the Spitzer Space Telescope. For modeling purposes we correct the K magnitudes for $H\alpha$ emission; the typical correction is 0.1 mag, but for 4/93 objects (Q2343-BX418, Q2343-BM133, Q1623-BX455, Q1623-BX502), it is $\gtrsim 0.4$ mag. We use a modeling procedure identical to that described in detail by Shapley et al. (2005), and review the method briefly here.

Photometry is fit with the solar metallicity Bruzual & Charlot (2003) models; as shown by Erb et al. (2006a), solar metallicity is a reasonable approximation for the massive galaxies in the sample, and more typical galaxies have metallicities only slightly less than solar. Although we use the models which employ a Salpeter (1955) IMF, it is well known that the steep faint-end slope of this IMF below $1 M_{\odot}$ overpredicts the mass-to-light ratio (M/L) and stellar mass by a factor of ~ 2 (e.g. Bell et al. 2003; Renzini 2005). For more accurate comparisons of stellar and dynamical masses we have therefore converted all stellar masses and star formation rates to the Chabrier (2003) IMF by dividing by 1.8 (a change in the faint end of the IMF affects only the inferred total stellar mass and star formation rate, because low mass stars do not contribute significantly to the flux in the observed passbands). Note that previous model SEDs of some of the same objects discussed here used the Salpeter IMF (Shapley et al. 2004, 2005).

The Calzetti et al. (2000) starburst attenuation law is used to account for dust extinction. We employ a variety of simple star formation histories of the form $\text{SFR} \propto e^{(-t_{\text{sf}}/\tau)}$, with $\tau = 10, 20, 50, 100, 200, 500, 1000, 2000$ and 5000 Myr, as well as $\tau = \infty$ (i.e. constant star formation, CSF). We also briefly consider more complex two component models, as described below; but as it is generally difficult to constrain the star formation histories even with simple models, we use only the single component models for the main analysis. For each galaxy we consider a grid of models with ages ranging from 1 Myr to the age of the Universe at the redshift of the galaxy, with extinctions ranging from $E(B - V) = 0.0$ to $E(B - V) = 0.7$, and with each of the values of τ listed above. We compare the $U_n\text{GRJK} + \text{IRAC}$ magnitudes of each model (shifted to the redshift of the galaxy) with the observed photometry, and determine the normalization which minimizes the value of χ^2 with respect to the observed photometry. Thus the reddening and age are determined by the model, and the star forma-

tion rate and total stellar mass by the normalization. In most cases all or most values of τ give acceptable values of χ^2 , while the constant star formation models give the best agreement with star formation rates from other indicators (see Erb et al. 2006b). For these reasons we adopt the CSF model unless it is a significantly poorer fit than the τ models. CSF models are used for 74 of the 93 objects modeled, and τ models for the remaining 19; as discussed by Shapley et al. (2005), the most massive galaxies, with $M_{\star} \gtrsim 10^{11} M_{\odot}$, are usually significantly better fit by declining models with $\tau = 1$ or 2 Gyr. Erb et al. (2006b) discuss this issue further. The adopted parameters and values of τ may be found in Table 3.

Parameters derived from this type of modeling are subject to substantial degeneracies and systematic uncertainties, primarily because of the difficulty in constraining the star formation history. These issues have been discussed in detail elsewhere (Papovich et al. 2001; Shapley et al. 2001, 2005). Here we simply note that age, reddening, and the value of τ suffer most from these degeneracies, and that the stellar mass is less sensitive to the assumed star formation history and thus more tightly constrained. We examine the effects of the assumed star formation history, and of photometric errors, through a series of Monte Carlo simulations which we use to determine uncertainties on the fitted parameters. The simulations are conducted as described by Shapley et al. (2005); the observed colors of the galaxy are perturbed by an amount randomly drawn from a Gaussian distribution with width determined by the photometric errors, and the best-fit SED is determined as usual for the perturbed colors, including the star formation history τ as a free parameter. We conduct 10,000 trials per object to estimate the uncertainties in each fitted parameter, and iteratively determine the mean and standard deviation of each parameter for each object, using 3σ rejection to suppress the effects of outliers. The resulting mean fractional uncertainties are $\langle \sigma_x / \langle x \rangle \rangle = 0.7, 0.5, 0.6$ and 0.4 in $E(B - V)$, age, SFR and stellar mass respectively. The distributions of $\sigma_x / \langle x \rangle$ are shown in Figure 3. The addition of the mid-IR IRAC data significantly improves our determination of stellar masses; for those objects with IRAC data (all those in the Q1700 and HDF fields) we find $\sigma_{M_{\star}} / M_{\star} \sim 0.2$, while those without the IRAC data have $\sigma_{M_{\star}} / M_{\star} \sim 0.5$. The IRAC data also reduce the uncertainties in the other parameters, though not by as large an amount. Shapley et al. (2005) show that while the IRAC data significantly reduce the uncertainties in stellar mass, the lack of these data does not substantially change or bias the inferred mass itself, especially when the K -band magnitude can be corrected for $H\alpha$ emission.

Confidence interval plots for M_{\star} vs. $E(B - V)$ and age vs. $E(B - V)$ for selected objects are shown in Figure 4, where the dark contours represent 68% confidence levels and the light 95%. The red \times marks our adopted best fit. The objects shown are representative of the range of properties spanned by the NIRSPEC sample. The first two objects, Q1623-BX502 and Q2343-BX493, have low stellar masses, young ages and relatively high values of $E(B - V)$. The third galaxy, Q1700-BX536, has properties close to the average of the sample, and also shows how much smaller the confidence intervals can become with the addition of the IRAC data. The last object,

Q2343-BX610, is a massive, old galaxy which can only be fit with $M_\star > 10^{11} M_\odot$ and age $t_{\text{sf}} > 1$ Gyr.

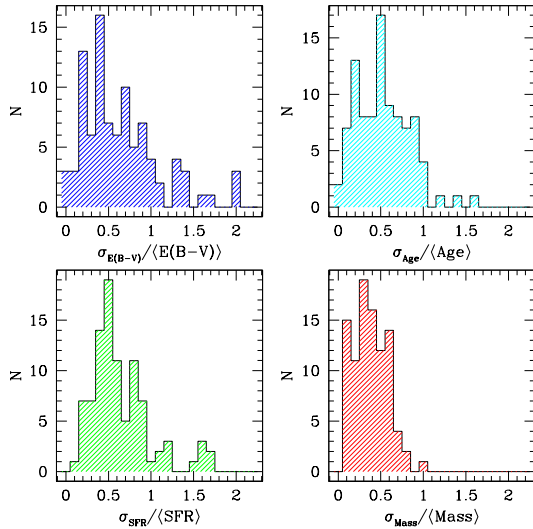


FIG. 3.— The distribution of uncertainties of each parameter fitted by our SED modeling code, from the Monte Carlo simulations described in the text. We show histograms of the ratio of the standard deviation to the mean of each parameter for all the objects modeled, determined iteratively with 3σ rejection. From left to right and top to bottom, we show $E(B - V)$, age, star formation rate, and stellar mass. Stellar masses are the best-constrained parameter, followed by the age of the star formation episode.

3.2. Model SED results

The best-fit parameters from the SED modeling are given in Table 3, and their distributions shown in the histograms in Figure 5. The mean stellar mass is $3.6 \pm 0.4 \times 10^{10} M_\odot$, and the median is $1.9 \pm 0.4 \times 10^{10} M_\odot$. The mean age is 1046 ± 103 Myr, and the median age is 570 ± 137 Myr. The sample has a mean $E(B - V)$ of 0.16 ± 0.01 and a median of 0.15 ± 0.01 . The mean SFR is $52 \pm 10 M_\odot \text{ yr}^{-1}$, while the median is $23 \pm 3 M_\odot \text{ yr}^{-1}$; the difference between the two reflects the fact that a few objects are best fit with high SFRs ($> 300 M_\odot \text{ yr}^{-1}$). We discuss the results of the models further in the following sections and in Erb et al. (2006b), where we compare them with properties determined from the H α spectra.

The 93 galaxies whose H α spectra and SEDs are discussed here are a subset of a larger sample of 461 objects with model SEDs. This larger sample will be discussed in full elsewhere (Erb et al. 2006, in preparation); for the moment we compare the distribution of stellar masses of the NIRSPEC galaxies with that of the full sample, which is representative of the UV-selected sample except that it excludes the $\sim 20\%$ of objects which are not detected to $K \sim 22.5$ (as discussed by Erb et al. (2006b), these are likely to be objects with low stellar masses and relatively low star formation rates). For the purposes of comparison with the full sample, we use models for the NIRSPEC galaxies in which we have not corrected the K magnitude for H α emission (since we do not have H α fluxes for the full sample); everywhere else in this paper, we use corrected K magnitudes for the modeling as described above. We also use CSF models for all galaxies

for this comparison. The distributions of stellar mass for the two samples are shown in Figure 6. The mean stellar mass of the subsample for which we have H α spectra is $3.7 \pm 0.5 \times 10^{10} M_\odot$; this is slightly higher than that of the full UV-selected sample which has a mean stellar mass of $3.0 \pm 0.5 \times 10^{10} M_\odot$, though the two are consistent within the uncertainties. A slightly higher average mass is expected for the NIRSPEC sample, since some of the galaxies were selected because of their bright K magnitudes or red $\mathcal{R} - K$ colors.

3.3. Two component models and maximum stellar masses

One limitation of this type of modeling is that it is sensitive to only the current episode of star formation; it is possible for the light from an older, underlying burst to be completely obscured by current star formation (Papovich et al. 2001; Yan et al. 2004; Shapley et al. 2005). Although we can only weakly constrain the star formation histories of individual galaxies even with simple declining models, more complex two-component models are a useful tool to assess how much mass could plausibly be missing. Two types of two-component models were used to examine this question. The first is a maximal mass model, in which we first fit the K -band (and IRAC, when it exists) data with a nearly instantaneous ($\tau = 10$ Myr), maximally old ($z_{\text{form}} = 1000$) burst, subtract this model from the observed data, and fit a young model to the (primarily UV) residuals. Such models produce stellar masses ~ 3 times higher than the single component models on average, but for galaxies with (single component) $M_\star \lesssim 10^{10} M_\odot$, the two component total masses are 10–30 times larger. Such models are poorer fits to the data, however, and are not plausible on average because the young components require extreme star formation rates; the average SFR for the young component of these models is $\sim 900 M_\odot \text{ yr}^{-1}$, $\gtrsim 30$ times higher than the average star formation rate predicted by the H α and UV emission (see Erb et al. 2006b). Nevertheless, we cannot rule out the possibility that such models may be correct for some small fraction of the sample.

We also use a more general two-component model, in which we fit a maximally old burst and a current star formation episode (of any age and with any of our values of τ) simultaneously, allowing the total mass to come from any linear combination of the two models. As expected given the number of free parameters, such models generally fit the data as well as or better than the single component models. They do not, however, usually significantly increase the total mass; the total two component mass is more than three times larger than the single component mass in only six cases. In general, then, the data do not favor models with large amounts of mass hidden in old bursts.

4. VELOCITY DISPERSIONS AND DYNAMICAL MASSES

The H α velocity dispersion σ reflects the dynamics of the gas in the galaxies' potential wells. Because it requires only a measurement of the line width, it can be determined for most of the objects in the sample; it is therefore our most useful kinematic quantity. Out of the 114 galaxies with H α detections, we measure a velocity dispersion from the H α line width for 85 objects.

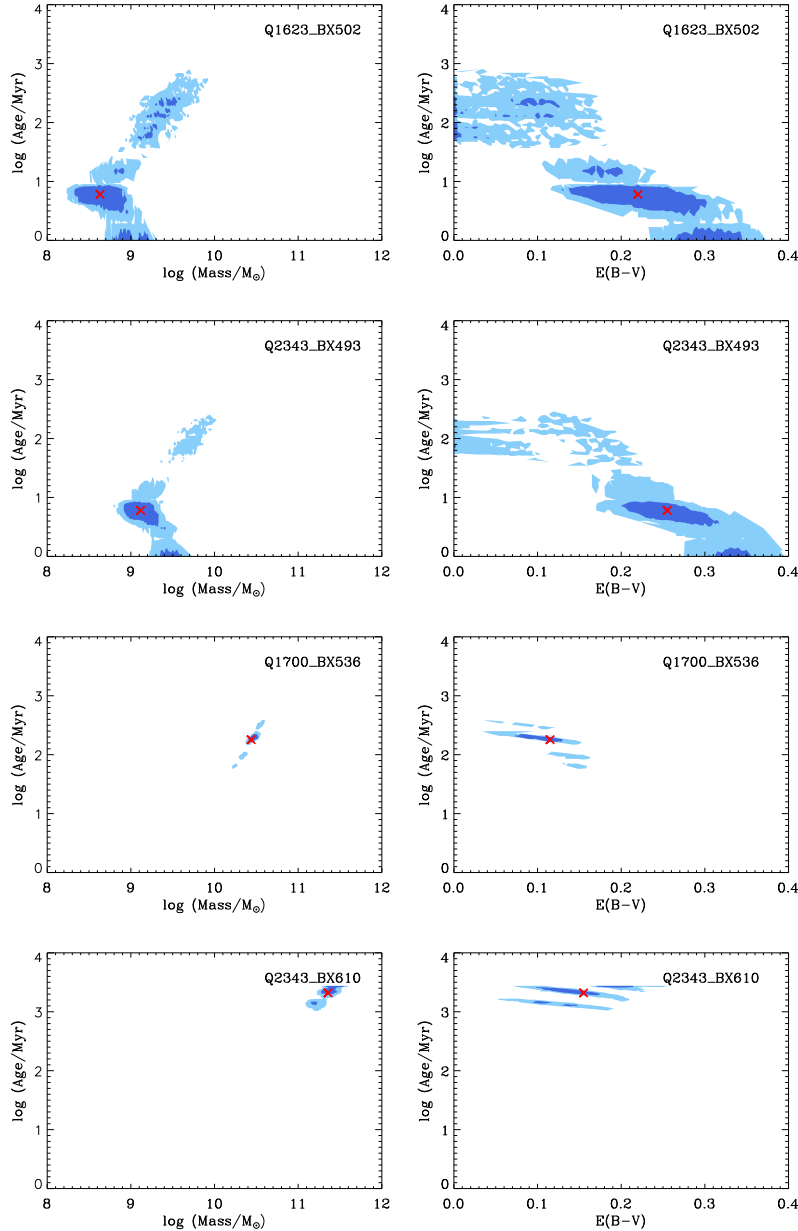


FIG. 4.— Sample confidence intervals for the fitted parameters, for four galaxies in the sample. Contours of stellar mass vs. age are shown on the left, and $E(B - V)$ vs. age on the right. The dark and light blue regions represent 68% and 95% confidence intervals respectively, and the red \times marks the adopted best fit. The top two objects are characteristic of the young, low stellar mass galaxies in the sample; the third row shows a typical galaxy, with fit very well-constrained by the addition of mid-IR IRAC data; and the bottom panel shows one of the most massive galaxies in the sample, which can only be fit by an old stellar population. Plots are shown with the same axes for ease of comparison.

For 11 additional objects we measure an upper limit on the velocity dispersion because the measured line width is not significantly higher than the instrumental resolution, as described below. 12 objects have FWHM less than the instrumental resolution due to noise, and 6 have been rejected due to significant contamination from night sky lines. We calculate the velocity dispersion $\sigma = \text{FWHM}/2.35$, where FWHM is the full width at half maximum after subtraction of the nominal instrumental resolution (15 \AA in the K-band) in quadrature. Uncertainties ($\Delta\sigma_{\text{up}}$ and $\Delta\sigma_{\text{down}}$) are determined by calculating σ_{max} and σ_{min} from the raw line width W and its statistical uncertainty ΔW ; $W + \Delta W$ gives σ_{max} and $W - \Delta W$ gives σ_{min} . This results in a larger lower bound

on the error when the line width is close to the instrumental resolution, and an upper limit on σ when $W - \Delta W$ is less than the instrumental resolution. In such cases we give one standard deviation upper limits of $\sigma + \Delta\sigma_{\text{up}}$. As we discuss further below, we have also measured the spatial extent of the $\text{H}\alpha$ emission for each object; for 14 objects, the $\text{FWHM}_{\text{H}\alpha}$ is less than the slit width. In such cases the effective resolution is increased by the ratio of the object size to the slit width; we have made this correction in the calculation of σ for these 14 objects. The correction is usually $< 10\%$.

Velocity dispersions are given in column 6 of Table 4. From the 85 measurements we find $\langle\sigma\rangle = 120 \pm 9 \text{ km s}^{-1}$ ($108 \pm 5 \text{ km s}^{-1}$ with AGN removed), with a standard

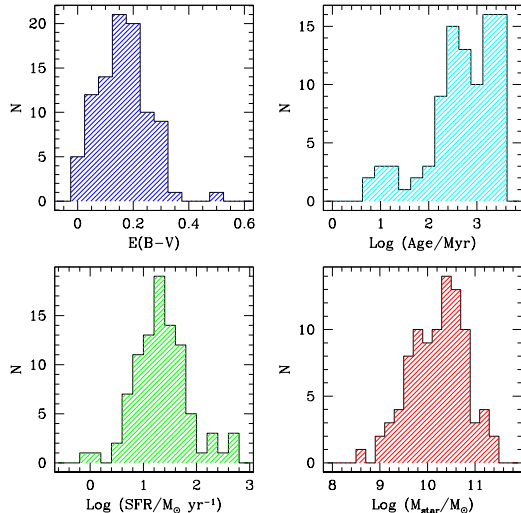


FIG. 5.— Histograms showing the distributions of the results of the SED modeling. From left to right and top to bottom, we show $E(B - V)$, age, star formation rate, and stellar mass. Statistics of the distributions are given in the text.

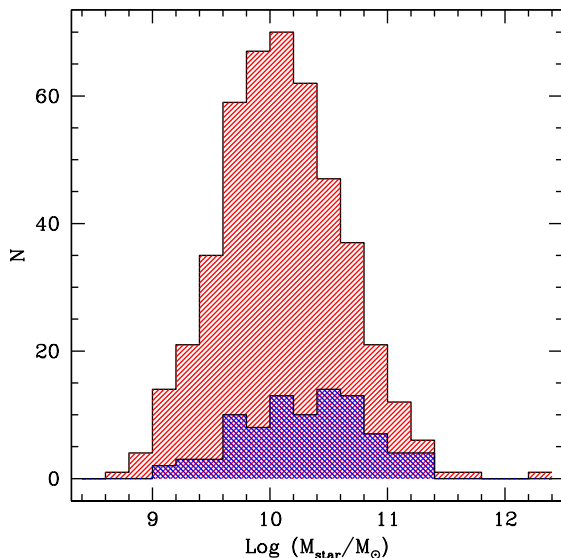


FIG. 6.— A comparison of the stellar masses of the full sample of 461 UV-selected galaxies (red) and the 93 galaxies for which we have model SEDs and $H\alpha$ spectra (blue). The mean stellar mass of the full sample is $3.0 \pm 0.5 \times 10^{10} M_{\odot}$, while that of the $H\alpha$ subsample is $3.7 \pm 0.5 \times 10^{10} M_{\odot}$. For the purposes of this comparison we use constant star formation models for all objects, and the K magnitudes of the NIRSPEC sample have not been corrected for $H\alpha$ emission.

deviation of 86 km s^{-1} , while counting the upper limits as detections gives $\langle \sigma \rangle = 112 \pm 9 \text{ km s}^{-1}$ ($101 \pm 5 \text{ km s}^{-1}$ without AGN) with a standard deviation of 85 km s^{-1} . The observed line widths could be caused by random motions, rotation, merging, or, most likely, some combination of all of these. Galactic outflow speeds (as measured by the velocity offsets between $H\alpha$, $\text{Ly}\alpha$, and the rest-frame UV interstellar absorption lines) show no correlation with the line widths, and the AGN fraction of $\sim 4\%$ means that broadening by AGN is usually not significant. Dynamical masses can be calculated from the line widths via the relation

$$M_{\text{dyn}} = C\sigma^2 r/G \quad (1)$$

The factor C depends on the galaxy’s mass distribution and velocity field, and may range from $C \leq 1$ to $C \geq 5$. The value of C depends on the mass density profile, the velocity anisotropy and relative contributions to σ from random motions or rotation, the assumption of a spherical or disk-like system, and possible differences in distribution between the total mass and that of tracer particles used to measure it. Obviously the definition of the radius r is also crucial. Most of these factors are unknown for the current sample.

Under the assumption that a disk geometry is appropriate for gas-rich objects (see §6), we begin with the relationship $M_{\text{dyn}} = v_{\text{true}}^2 r/G$. We incorporate an average inclination correction $\langle v_{\text{true}} \rangle = \pi/2 \langle v_{\text{obs}} \rangle$, and for v_{obs} use the observed velocity half-width ($v_{\text{obs}} = \text{FWHM}/2 = 2.35\sigma/2$). Combining the constants and writing the equation in terms of σ then gives $C \simeq 3.4$. For the galaxy size $r_{H\alpha}$ we use half of the spatial extent of the $H\alpha$ emission, after deconvolution of the seeing. The galaxies are spatially resolved in almost all cases; for those few that are not, we use the smallest size measured under the same seeing conditions as an upper limit. We find a mean and standard deviation $\langle r_{H\alpha} \rangle = 0.7 \pm 0.3''$ ($\sim 6 \text{ kpc}$), approximately the same as the typical isophotal radius used for photometric measurements. Because it is difficult to continuously monitor the seeing while observing with NIRSPEC, some uncertainty is introduced by our inexact knowledge of the seeing during each observation. This uncertainty is typically $0.1\text{--}0.2''$, but for those objects that are near the resolution limit it may be much larger. Because of this issue, the sizes are uncertain by $\sim 30\%$. Note that most previous calculations of dynamical mass at high redshift have used $C = 5$ (appropriate for a uniform sphere; e.g. Pettini et al. 2001; Erb et al. 2003, 2004; Shapley et al. 2004; van Dokkum et al. 2004; Swinbank et al. 2004).

Values of $r_{H\alpha}$ are given in column 5 of Table 4, and dynamical masses in column 8. Using the 85 galaxies with well-determined σ , we find a mean dynamical mass $\langle M_{\text{dyn}} \rangle = 1.2 \pm 0.4 \times 10^{11} M_{\odot}$. The two largest dynamical masses in the sample are $M_{\text{dyn}} = 5.7 \times 10^{11} M_{\odot}$ (Q1700-MD174) and $M_{\text{dyn}} = 3.8 \times 10^{12} M_{\odot}$ (Q1700-MD94); both of these objects are AGN, and their broad $H\alpha$ lines are therefore not a reflection of the gravitational potential. Neglecting these two objects, and the other AGN which have $M_{\text{dyn}} \sim 6 - 9 \times 10^{10} M_{\odot}$ (HDF-BMZ1156, Q1623-BX151 and Q1623-BX663), results in $\langle M_{\text{dyn}} \rangle = 6.9 \pm 0.6 \times 10^{10} M_{\odot}$, with a standard deviation of $5.8 \times 10^{10} M_{\odot}$. Approximately 25% of the non-AGN have dynamical masses $M_{\text{dyn}} > 10^{11} M_{\odot}$, with Q1623-BX376 ($M_{\text{dyn}} = 3.7 \times 10^{11} M_{\odot}$) the largest.

Uncertainties in the dynamical masses are probably dominated by the constant C , which may vary by a factor of a few. Our line widths may also occasionally suffer from contamination by night sky lines; we have removed the most obvious cases, but repeated observations with varying signal-to-noise ratios (S/N) show that this can occasionally affect the line profile by up to $\sim 30\%$. Complex spatial and kinematic structure can also affect the observed velocity dispersion, as discussed previously (Erb et al. 2003) and recently emphasized by Colina et al. (2005). The $H\alpha$ emission also may not trace the full potential, especially in low S/N spectra of high

redshift objects. Even in some local starburst galaxies the H α emission does not fully sample the rotation curve (Lehnert & Heckman 1996). Indeed, the mean dynamical mass we derive here is ~ 15 times lower than the typical halo mass as inferred from the galaxies' clustering properties (Adelberger et al. 2005b).

4.1. Comparisons with Stellar Masses

Turning next to a comparison of the galaxies' dynamical and stellar masses, in Figure 7 we plot dynamical mass vs. stellar mass for the 68 galaxies for which we have determined both. The dashed line shows equal masses, while the dotted lines on either side indicate approximate uncertainties of ± 0.8 dex (a $\sim 50\%$ uncertainty in both masses, added in quadrature; this includes systematic uncertainties in the dynamical mass model as well as the measurement uncertainties shown by the error bars in the lower right corner). Excluding AGN, the mean dynamical mass is ~ 2 times higher than the mean stellar mass. Significant correlation between stellar and dynamical mass is observed in the local universe (e.g. Brinchmann & Ellis 2000), but such a correlation will exist only if the stellar mass makes up a relatively constant fraction of the dynamical mass over the full range of stellar masses. If low stellar mass galaxies have large gas fractions, as is seen in local galaxies (McGaugh & de Blok 1997; Bell & de Jong 2000), they may not have correspondingly small dynamical masses. With these caveats in mind, we perform Spearman and Kendall τ correlation tests (neglecting the AGN) and find a probability $P = 0.01$ that the masses are uncorrelated, for a significance of the correlation of 2.5σ . This is consistent with our qualitative expectations from Figure 7, where most of the points lie well within the dotted lines marking a factor of ~ 6 difference between the masses (though we see a significant number of outliers with $M_{\text{dyn}} \gg M_*$, to be discussed further below).

Approximately 20% of the galaxies in the sample have $M_* > M_{\text{dyn}}$, clearly an unphysical situation. The discrepancies are usually a factor of 2–3 and always less than a factor of ~ 6 , which can be easily explained by the factor of a few uncertainty in both masses. In any case, because the H α linewidths may not sample the full potential it would not be a surprise to find some objects with $M_* > M_{\text{dyn}}$.

It is potentially more interesting to consider the small but significant fraction of the objects for which $M_{\text{dyn}} \gg M_*$; we focus on the $\sim 15\%$ of the sample (11/68) for which $M_{\text{dyn}}/M_* > 10$ (one of these is the AGN Q1700-MD94, which has a dynamical mass of $3.8 \times 10^{12} M_\odot$ due to its very broad H α line; this is clearly a problematic estimate of dynamical mass, and we exclude this object in the following discussion). These objects are marked with open diamonds in Figure 7, and in many of the subsequent figures as well. The large differences between stellar and dynamical masses suggest the following possibilities: 1) these are galaxies that have recently begun forming stars, and thus have small stellar masses and large gas fractions; or 2) we significantly underestimate the stellar mass for up to $\sim 15\%$ of the sample, presumably because of an undetected old stellar population. One should also consider the possibility that contamination from winds, shock ionization or AGN causes an overestimate of the dynamical masses of $\sim 15\%$ of

the sample. There is no evidence for this third possibility, however; except in the few cases of known AGN, none of the objects show evidence of ionization from any source other than star formation, either from their UV spectra or from high [N II]/H α ratios. The objects with $M_{\text{dyn}} \gg M_*$ have low stellar masses, and as Erb et al. (2006a) show in the context of estimating metallicity as a function of stellar mass, [N II] is not detected even in a composite spectrum of 15 such objects.

The best fit ages and H α equivalent widths (Erb et al. (2006b) discuss the equivalent widths more fully) of the set of galaxies with $M_{\text{dyn}}/M_* > 10$ favor the first possibility. As shown in Figure 8, there is a strong correlation between M_{dyn}/M_* and age, and, with somewhat more scatter, between M_{dyn}/M_* and $W_{\text{H}\alpha}$ (the correlations have 5 and 4 σ significances respectively). Objects with $M_{\text{dyn}} \gg M_*$ have young best fit ages, and tend to have high H α equivalent widths as well, with $200 \lesssim W_{\text{H}\alpha} \lesssim 1300 \text{ \AA}$. Note that these are not correlations of independent quantities; age and stellar mass are correlated by definition in the constant star formation models we use for the majority of the sample, and the equivalent width depends on the K_s magnitude, which is also closely related to stellar mass. This, combined with the fact that we see less dispersion in dynamical mass than stellar mass, accounts for the correlations in Figure 8.

It is important to assess whether or not the $M_{\text{dyn}} \gg M_*$ galaxies are really significantly younger than the rest of the sample, given the well-known degeneracies between age and extinction in SED modeling and the considerable uncertainties in the age of a typical object. Confidence intervals for the age– $E(B - V)$ fits for two of the $M_{\text{dyn}} \gg M_*$ galaxies (Q1623-BX502 and Q2343-BX493) are shown in Figure 4. These are representative of this set of objects. Young ages (and correspondingly high values of $E(B - V)$) are clearly strongly favored, but there is a tail of acceptable solutions extending to higher ages. This set of objects is unique in favoring such young ages. To further test the significance of the young ages, we have divided the sample into four quartiles by M_{dyn}/M_* (with 16, 17, 17 and 17 galaxies in the quartiles), and performed K-S tests on the age distribution of each quartile, making use of the Monte Carlo simulations described in §3. These simulations perturb the colors of each galaxy according to its photometric errors, and compute the best-fit model for the perturbed colors. We conducted 10,000 trials for each galaxy, and generated lists of the best-fit ages for all trials in each quartile (for 160,000 or 170,000 trial ages in each quartile). A two sample K-S test on all pairs of the four quartiles finds that the probability $P \simeq 0$ that the ages in the quartile with the highest M_{dyn}/M_* are drawn from the same distribution as the remaining quartiles. This test suggests that even though the ages of individual galaxies may not be well constrained, the younger average age of the subsample with $M_{\text{dyn}} \gg M_*$ is highly significant.

The best-fit ages from the SED fitting represent the age of the current star formation episode, however, not necessarily the galaxy as a whole, which brings us to possibility 2) above: is there a significant underlying population of old stars in these objects which causes us to underestimate the stellar mass? We address this question through the two-component models described in §3.3,

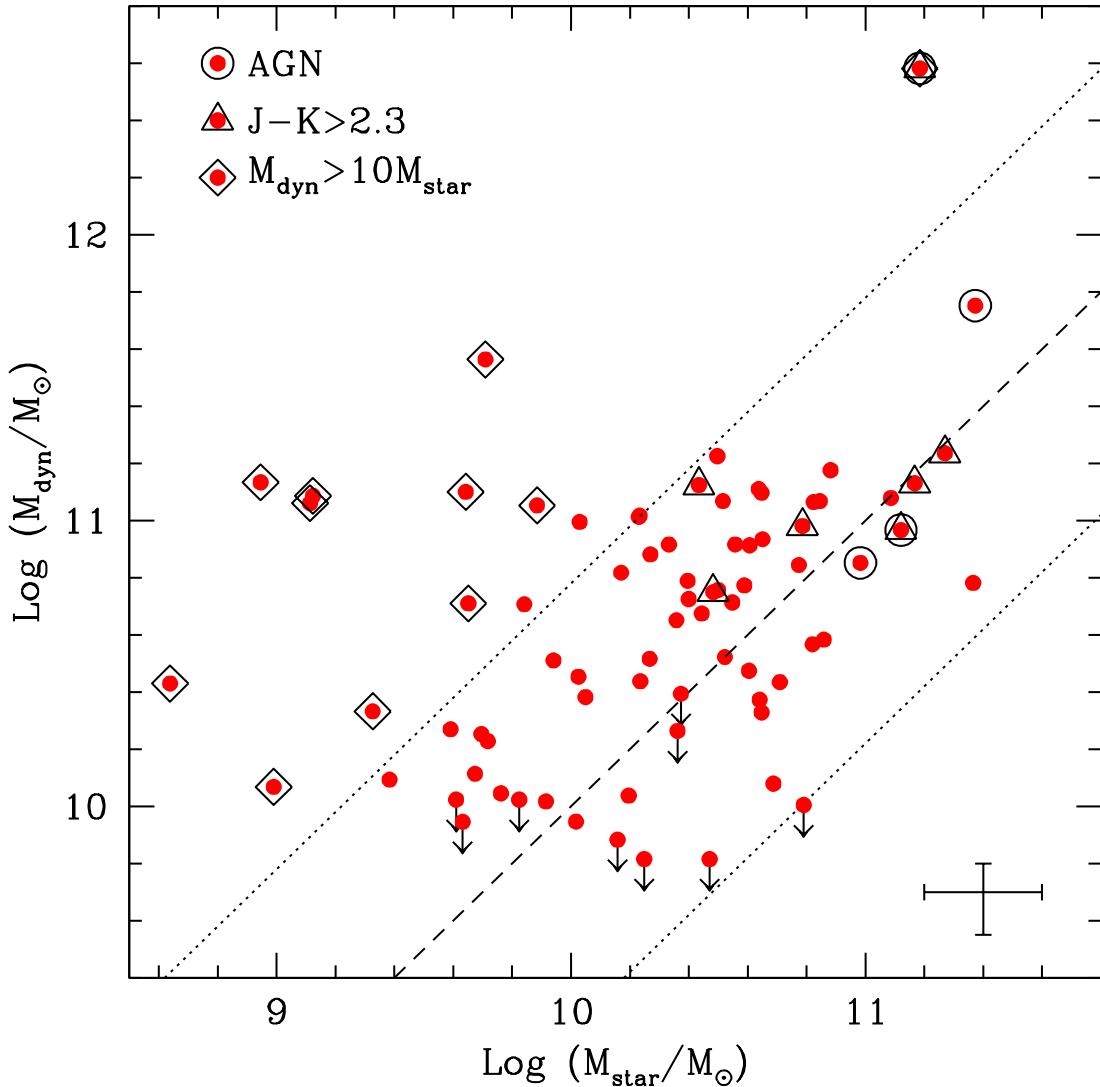


FIG. 7.— Dynamical vs. stellar mass for the 68 galaxies with measurements of both quantities. Excluding AGN, we find $\langle M_\star \rangle = 3.5 \pm 0.5 \times 10^{10} M_\odot$, while the mean dynamical mass is $\langle M_{\text{dyn}} \rangle = 7.1 \pm 0.7 \times 10^{10} M_\odot$. The dashed line indicates equal masses. The error bars in the lower right corner show typical uncertainties, which for dynamical masses include only measurement errors in $r_{\text{H}\alpha}$ and σ . Uncertainties in dynamical masses are dominated by the unknown factors in the mass model as discussed in the text; incorporating these uncertainties, we estimate approximate combined uncertainties of ~ 0.8 dex, as shown by the dotted lines. Galaxies with $M_{\text{dyn}}/M_\star > 10$ are marked with open diamonds, and we discuss possible reasons for their discrepancy in the text.

which fit the SED with the superposition of a young burst and maximally old population to estimate the maximum stellar mass. The maximal mass models, which fit all the flux redward of the K -band with an old burst, and then fit a young model to the UV residuals, result in stellar masses ~ 5 – 30 times larger for those galaxies with $M_{\text{dyn}}/M_\star > 10$. If we use the maximal mass models for these objects rather than the single-component models in the comparison with dynamical mass, we find $\langle M_{\text{dyn}}/M_\star \rangle = 3$, as compared to $\langle M_{\text{dyn}}/M_\star \rangle = 54$ using the single component models. However, as described in §3.3, these models are poorer fits and result in implausibly high average SFRs. A further difficulty is that the mean age of the young component in these models is 3.5 Myr, approximately 1/20 the typical dynamical timescale for these galaxies. The more general two-component modeling, in which the total mass comes from

a varying linear combination of a maximally old burst and an episode of current star formation, does not favor such extreme models; for the $M_{\text{dyn}} \gg M_\star$ galaxies in question, the use of these more general models increases the average stellar mass by a factor of three.

More powerful constraints on the ages and masses of the $M_{\text{dyn}} \gg M_\star$ objects come from the spectra of the galaxies themselves. Using composite spectra of the current sample, Erb et al. (2006a) show that there is a strong trend between metallicity and stellar mass in the $z \sim 2$ sample, such that the lowest stellar mass galaxies also have low metallicities. These objects likely have large gas fractions, accounting for their relatively low metal content (we discuss the derivations of the gas fractions further in §6). These results strongly favor the hypothesis that the large dynamical masses of these objects are due to a large gas mass rather than a significant

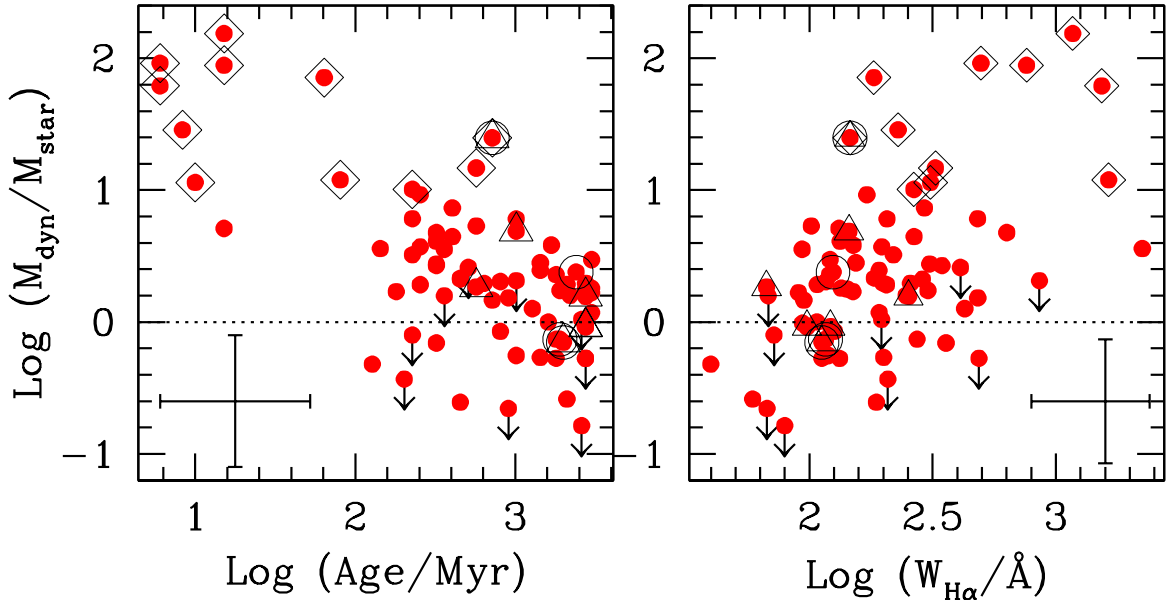


FIG. 8.— Left: The mass ratio M_{dyn}/M_{\star} vs. the best-fit age from SED modeling, and right, M_{dyn}/M_{\star} vs. $H\alpha$ equivalent width $W_{H\alpha}$. Galaxies with high M_{dyn}/M_{\star} have young ages, and also tend to have high equivalent widths. Typical uncertainties are shown by the error bars in the corner of each plot. Symbols are as in Figure 7.

population of old stars. From both considerations of dynamical mass and baryonic mass (gas and stars, §6), it seems clear that objects with a best-fit *stellar* mass of $M_{\star} \lesssim 10^9 M_{\odot}$ are not in fact significantly less massive than the rest of the sample.

4.2. Velocity Dispersion and Optical Luminosity

The correlation between the luminosity of elliptical galaxies and their velocity dispersion σ (the Faber–Jackson relation, $L \propto \sigma^4$; Faber & Jackson 1976) is well-established in the local universe. Many proposals for the origin of this correlation rely on self-regulating feedback processes; for example, Murray et al. (2005) propose that momentum-driven winds from supernovae and radiation pressure regulate the luminosity from star formation at $L \propto \sigma^4$. Other theories (e.g. Begelman & Nath 2005; Robertson et al. 2005 and references therein) use feedback from accretion onto a supermassive black hole to produce a correlation between luminosity or stellar mass and velocity dispersion as a byproduct of the relationship between black hole mass and velocity dispersion, $M_{\text{BH}} \propto \sigma^4$ (Ferrarese & Merritt 2000; Gebhardt et al. 2000; Tremaine et al. 2002). In the local universe, these correlations exist in relatively homogeneous, quiescent galaxies; with the present data, we can test the relationships between luminosity, stellar mass and velocity dispersion at a time in which the galaxies are building up much of their stellar mass.

Previous efforts to find such relations at high redshift have generally suffered from small sample sizes and resulted in weak or absent correlations with large amounts of scatter (Pettini et al. 2001; van Dokkum et al. 2004; Swinbank et al. 2004). We revisit the relation between σ and optical luminosity with a sample of 77 $z \sim 2$ UV-selected galaxies, augmented by 21 SCUBA galaxies presented by Swinbank et al. (2004), four of the Distant Red Galaxies (DRGs) discussed by van Dokkum et al. (2004), and 16 Lyman-break galaxies at $z \sim 3$ (Pettini et al. 2001 give velocity dispersions for nine galaxies observed

in K and (usually) J by Shapley et al. 2001, and we have subsequently observed seven more). Our total sample thus consists of 118 galaxies with a mean spectroscopic redshift $\langle z \rangle = 2.38$ and $\sigma_z = 0.37$.

Figure 9 shows the extinction-corrected rest-frame V -band luminosity plotted against the velocity dispersion σ ; the luminosity is determined by multiplying the best-fit SED with the redshifted V transmission curve, and the extinction correction employs the Calzetti et al. (2000) extinction law and the best-fit values of $E(B - V)$ from the SED modeling. We have used photometry from Shapley et al. (2001) to re-model the SEDs of the $z \sim 3$ LBGs, for consistency with the $z \sim 2$ sample. We also use the extinction-corrected magnitudes M_V from Swinbank et al. (2004), and use the values of A_V determined from SED modeling by van Dokkum et al. (2004) to correct their absolute V magnitudes. The solid line shows the local i -band⁷ Faber–Jackson relation derived from 9000 Sloan Digital Sky Survey (SDSS) galaxies by Bernardi et al. (2003). Assuming no change in slope, the local relation is offset from the median of the data by 1.35 dex in luminosity, as shown by the dotted line. The data are strongly correlated; the Spearman and Kendall τ tests give a probability $P = 2 \times 10^{-5}$ that the data are uncorrelated, for a significance of 4.1σ . An attempt to fit both the slope and the zeropoint of the correlation shows that the slope is not well-constrained, and depends strongly on the fitting procedure and the relative uncertainties assumed for L and σ ; however, it is not inconsistent with ~ 4 , the observed slope of the local Faber–Jackson relation.

Though there is strong evidence for a correlation between L and σ at $z > 2$, the scatter is considerable and too large to be accounted for by observational errors. σ varies by a factor of ~ 3 – 4 at a given luminosity, and for most values of σ we see at least an order of mag-

⁷ The slope of the Faber–Jackson relation is the same within the uncertainties in all bands, while the zeropoint decreases slightly at shorter wavelengths.

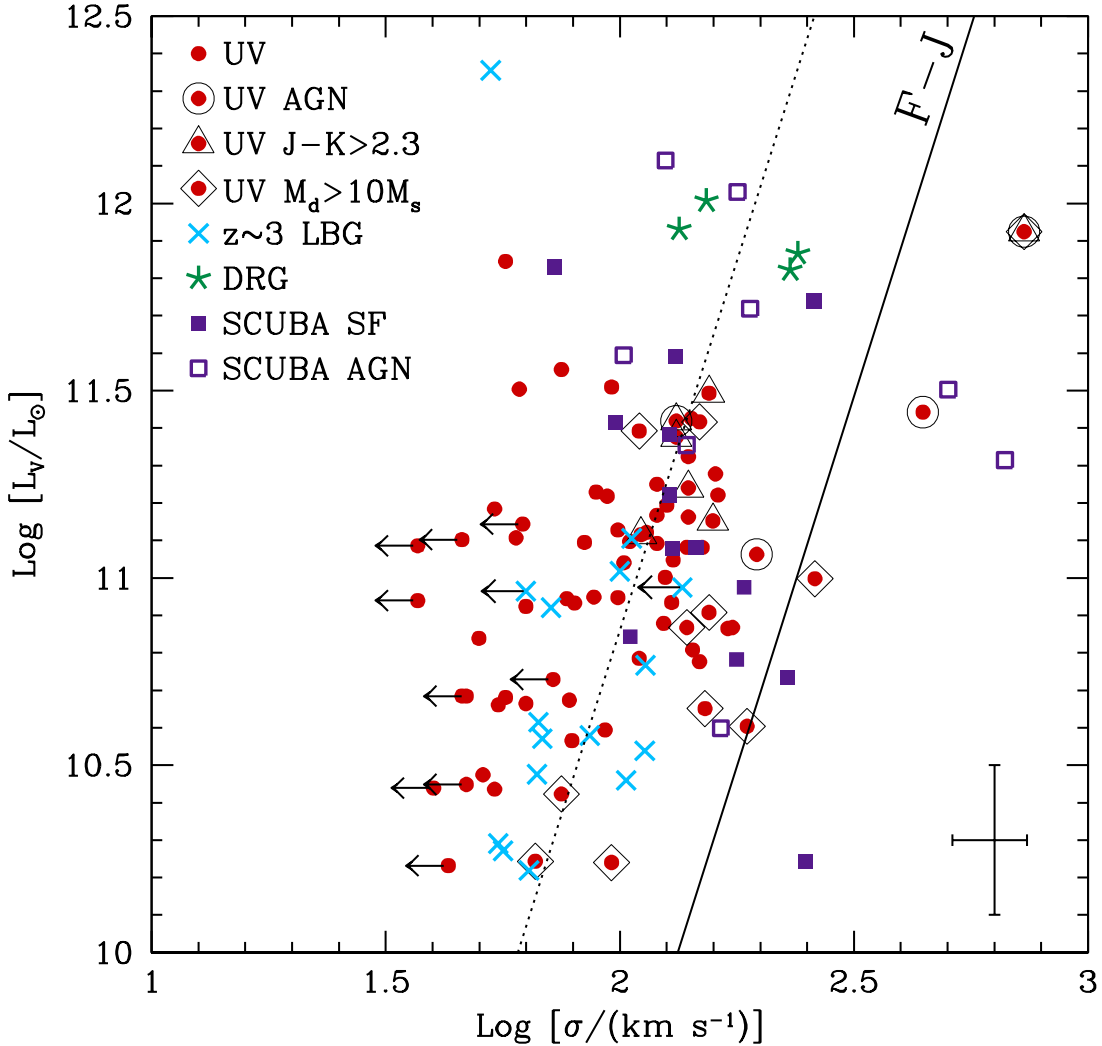


FIG. 9.— Velocity dispersion vs. extinction-corrected rest-frame V-band luminosity. Red circles show the current sample, blue \times s are Lyman break galaxies at $z \sim 3$, green stars are the DRGs presented by van Dokkum et al. (2004), and the purple squares represent the SCUBA galaxies of Swinbank et al. (2004, filled squares are those classified as star-forming galaxies, and open squares represent AGN). The solid line shows the local Faber-Jackson relation, and the dotted line shows the local relation shifted upward by 1.35 dex in order to pass through the median of the data. Typical uncertainties are shown by the error bars in the lower right corner.

nitide variation in L . Some insight into the sources of the scatter may be obtained by accounting for the large variation in the mass-to-light ratio M/L observed at $z \sim 2$. As shown by Shapley et al. (2005) for a similar sample of UV-selected galaxies, the rest-frame optical M/L varies by a factor of ~ 80 , with the highest values of M/L approaching the typical values seen in local galaxies; we find very similar results for the current sample. In Figure 10 we account for this variation by decreasing the luminosity of each galaxy in the $z \sim 2$ sample by the difference between its value of M/L and the typical $(M/L)_0$ of an elliptical galaxy in the local universe. We use $(M/L)_0 = 3$, as found by Padmanabhan et al. (2004) for elliptical galaxies in the SDSS; the average shift in luminosity is a factor of 10, and the shift ranges from a factor of 2 to a factor of 120. The figure approximates what would be observed at $z \sim 0$ if each galaxy were fixed at its current stellar mass and velocity dispersion and faded to

match present-day M/L values. This prediction is particularly relevant for the current sample because the clustering properties of the $z \sim 2$ galaxies indicate that they are the likely progenitors of elliptical galaxies like those seen in the SDSS (Adelberger et al. 2005b). The solid line again shows the local Faber-Jackson relation, which is a reasonable fit to many of the points; however, the large remaining scatter and significant number of outliers are consistent with the expectation (from the high gas fractions discussed in §6 and the high SFRs found by Erb et al. 2006b) that most of the galaxies are still actively building up stellar mass.

For the current data, the most relevant prediction of the relationship between L and σ at high redshift is that of Murray et al. (2005), who propose a limiting, Eddington-like luminosity for starbursts, $L_M \simeq (4f_g c/G)\sigma^4$, where f_g refers to the gas fraction. In this model, momentum-driven winds powered by radiation

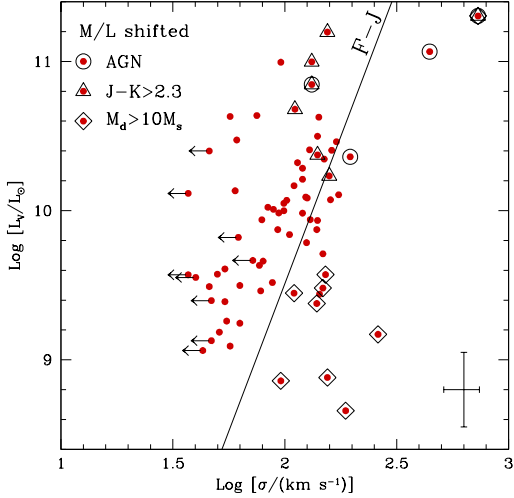


FIG. 10.— The V-band luminosities of the $z \sim 2$ sample shifted by the difference between the observed and local mass-to-light ratios as described in the text, plotted vs. velocity dispersion σ . The solid line shows the local Faber-Jackson relation. Typical uncertainties are shown by the error bars in the lower right corner.

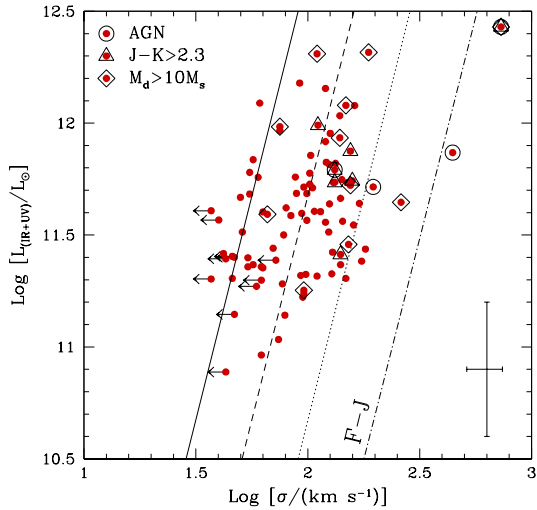


FIG. 11.— Bolometric luminosity $L_{(\text{IR}+\text{UV})}$ calculated from the extinction-corrected $\text{H}\alpha$ star formation rates as described in the text vs. velocity dispersion, compared with the model of Murray et al. (2005) for gas fractions $f_g = 1.0, 0.1,$ and 0.01 (solid, dashed and dotted lines respectively). These three lines also indicate reasonable uncertainties in the model. The local Faber-Jackson relation is shown by the dot-dash line at right. Typical uncertainties are shown by the error bars in the lower right corner.

pressure and supernovae would expel much of the gas from the galaxy at luminosities above L_M . At L_M , feedback moderates the SFR, and luminosity does not increase significantly beyond L_M . L_M represents the bolometric luminosity from star formation, so the plot of L_V vs. σ discussed above is not the most appropriate test of this prediction. Instead we estimate the bolometric luminosities $L_{(\text{IR}+\text{UV})}$ from the extinction-corrected $\text{H}\alpha$ SFRs determined by Erb et al. (2006b). We invert the prescription of Bell et al. (2005), who relate the star formation rate to the bolometric luminosity, to produce the

following relation:

$$L_{(\text{IR}+\text{UV})}/L_{\odot} = 1.0 \times 10^{10} \text{ SFR}/M_{\odot} \text{ yr}^{-1}. \quad (2)$$

Here L_{IR} represents the total IR luminosity, while L_{UV} is the light from unobscured stars. Before using this expression we have converted our SFRs to the Kroupa (2001) IMF used by Bell et al. (2005). We find a mean $\langle L_{(\text{IR}+\text{UV})} \rangle = 4.6 \times 10^{11} L_{\odot}$, slightly higher than the average bolometric luminosity $\langle L_{(\text{IR}+\text{UV})} \rangle = 2.3 \times 10^{11} L_{\odot}$ estimated for a different sample of UV-selected $z \sim 2$ galaxies from $24 \mu\text{m}$ observations by Reddy et al. (2006). The two determinations of $L_{(\text{IR}+\text{UV})}$ can be compared directly for 11 galaxies common to both samples, as shown in Figure 5 of Reddy et al. (2006); the two measurements agree within the uncertainties, with $\langle \log L_{\text{bol}}^{\text{H}\alpha} \rangle = 11.46 \pm 0.27$ and $\langle \log L_{\text{bol}}^{\text{IR}+\text{UV}} \rangle = 11.59 \pm 0.20$.

Figure 11 shows the inferred bolometric luminosity $L_{(\text{IR}+\text{UV})}$ plotted against velocity dispersion, along with lines indicating L_M for gas fractions $f_g = 1.0, 0.1,$ and 0.01 (from left to right, solid, dashed and dotted lines). We also show the local Faber-Jackson relation. Although the three L_M lines indicate differences in the gas fraction, they also represent the uncertainty in L_M . They are not sufficient to discriminate between gas fractions; the objects with the highest inferred gas fractions (the $M_{\text{dyn}} \gg M_{\star}$ galaxies marked with open diamonds) do not fall closest to the $f_g = 1.0$ line. Within these uncertainties, the Murray et al. (2005) model appears to be a reasonable description of the data; the points are strongly correlated, with 4.0σ significance and $P = 7 \times 10^{-5}$, and the L_M lines bracket most of them.

The observed or inferred luminosity is a complex superposition of light from current star formation and from formed stellar mass (and from dust emission, in the case of bolometric luminosities), and the star formation rate likely varies on a much shorter timescale than σ . A somewhat less complicated comparison may therefore be between stellar mass and velocity dispersion, quantities that might be expected to be related through the $M_{\text{BH}} - \sigma$ relation and the $M_{\text{bulge}} - M_{\text{BH}}$ relation (Magorrian et al. 1998; Marconi & Hunt 2003) as well as through the comparison of stellar and dynamical masses discussed above. We plot stellar mass M_{\star} vs. σ in Figure 12; this is similar to Figure 7, although here we add the $z \sim 3$ LBGs and the DRGs. The correlation has a significance of 3.6σ , about the same as the $\sigma - L$ correlation; the low stellar mass galaxies with large velocity dispersions discussed above are clear outliers (marked with open diamonds; they are included in the above correlation test). The dotted line is the local relation between bulge stellar mass and velocity dispersion, constructed by combining the $M_{\text{bulge}} - M_{\text{BH}}$ relation of Marconi & Hunt (2003) and the $M_{\text{BH}} - \sigma$ relation of Tremaine et al. (2002); it provides a surprisingly accurate upper envelope in σ on the plot, as with the exception of AGN and the $M_{\text{dyn}} \gg M_{\star}$ objects discussed above (marked with open diamonds), virtually all of the points lie on or to the left of this line.

At least some theoretical predictions indicate that the correlation between M_{\star} and σ should be strong at high redshift. The results of one such study are shown by the open symbols, from the numerical simulations of Robertson et al. (2005, see their Figure 3). These simulations test the evolution of the $M_{\text{BH}} - \sigma$ relation with red-

shift using simulations of merging galaxies, incorporating feedback from black hole growth such that $\sim 0.5\%$ of the accreted rest mass energy heats the gas. The $M_{BH} - \sigma$ correlation then results from the regulation of black hole growth by feedback (Di Matteo et al. 2005). The simulation results for $z = 2$ (open squares) and $z = 3$ (open circles) describe the upper envelope in observed σ reasonably well, but the data exhibit considerably more scatter. Given the parameters of the simulations, this is not a surprise. The velocity dispersions in the models (which are the stellar velocity dispersions, not the gas velocity dispersions we use) are measured well after the merger and accompanying AGN feedback, when the star formation rate has dropped to nearly zero (Di Matteo et al. 2005), while the data represent galaxies at a variety of stages of an earlier starburst phase. The simulation sample is therefore considerably more homogeneous than the data set.

A large number of galaxies in our data set have low velocity dispersions for their stellar mass relative to the local correlation (or high stellar mass for their velocity dispersion). In fact this is the opposite of the trend predicted by the simulations, which indicate weak evolution with redshift in the $M_{BH} - \sigma$ and $M_* - \sigma$ relations, in the sense that velocity dispersions increase at a given stellar mass at higher redshifts (attributed to the steeper potential wells of high redshift galaxies). This difference may reflect the fact that we are probably underestimating the true velocity dispersion in many cases, since we are only sensitive to the highest surface brightness star-forming regions, which may not sample the full potential. It will be interesting to see if deeper spectra with larger telescopes result in a higher average velocity dispersion for this sample, and an accompanying reduction of the scatter. This plot also provides a hint of an evolutionary sequence: if the $M_{dyn}/M_* > 10$ objects are indeed young galaxies with high gas fractions, they may evolve upward on this plot, significantly increasing their stellar mass with relatively little change in velocity dispersion until they fall on or to the left of the dotted line along with the rest of the sample. It is also possible that the velocity dispersions of these objects will *decrease* over time, bringing them closer to the local relation, if they lose a large fraction of their gas to outflows (as suggested by Erb et al. 2006a). From the observed correlations of σ , L , and M_* , and their accompanying scatter, we conclude that the processes which create correlations between these properties in the local universe are underway at $z \sim 2$.

4.3. A Comparison with $z \sim 3$ Lyman Break Galaxies

Close examination of Figure 9 shows that the velocity dispersions of the $z \sim 2$ sample and the $z \sim 3$ LBGs have different distributions. We compare the two directly in Figure 13, which shows histograms of the velocity dispersions of the $z \sim 2$ galaxies and the LBGs, after excluding AGN. The mean and the error in the mean of the $z \sim 2$ sample is $\langle \sigma \rangle = 108 \pm 5 \text{ km s}^{-1}$, while for the $z \sim 3$ LBGs it is $\langle \sigma \rangle = 84 \pm 5 \text{ km s}^{-1}$; the difference between the two means is of 5σ significance. The $z \sim 2$ distribution is significantly broader; objects with low velocity dispersions are common at $z \sim 2$ as well as at $z \sim 3$, but the lower redshift sample contains a large number of objects with $\sigma \gtrsim 130 \text{ km s}^{-1}$. Only one such galaxy is present in the

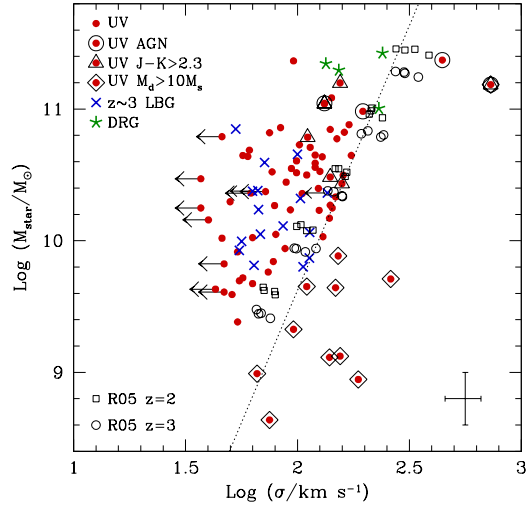


FIG. 12.— Stellar mass vs. velocity dispersion. The dotted line shows the local relation between bulge stellar mass and velocity dispersion, constructed by combining the $M_{bulge} - M_{BH}$ relation of Marconi & Hunt (2003) and the $M_{BH} - \sigma$ relation of Tremaine et al. (2002). Open squares and circles show the results of the simulations of Robertson et al. (2005), which test the evolution of the $M_{BH} - \sigma$ relation with redshift. Typical uncertainties are shown by the error bars in the lower right corner.

$z \sim 3$ sample. The $z \sim 3$ galaxies have an average dynamical mass $\langle M_{dyn} \rangle = 3.6 \pm 0.6 \times 10^{10} M_{\odot}$, a factor of two smaller than that of the $z \sim 2$ galaxies; the average stellar mass of the LBGs is also a factor of ~ 2 lower than that of the $z \sim 2$ galaxies (Shapley et al. 2001), though this comparison is complicated by sample selection effects. As described in detail below, these differences in velocity dispersion and dynamical mass appear to reflect real differences between the $z \sim 2$ and $z \sim 3$ samples.

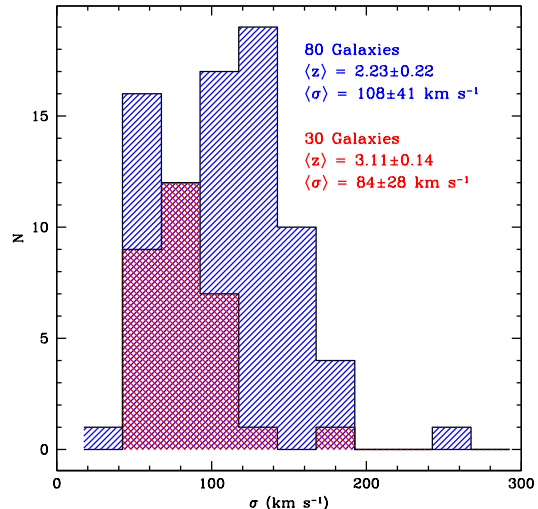


FIG. 13.— The distributions of the velocity dispersions of $z \sim 2$ (larger blue histogram) and $z \sim 3$ (smaller red histogram) galaxies. At $z \sim 2$, σ is derived from the width of the $H\alpha$ emission line, while $[O III]$ is used for the $z \sim 3$ sample.

Possible selection effects are a concern in attempting to understand the different distributions of σ in the two samples. The $z \sim 3$ line widths are measured from

[O III] λ 5007, while H α is used for the $z \sim 2$ galaxies. To see if systematic differences between line widths measured from the two lines might be responsible for the effect, we have measured line widths from [O III] λ 5007 for 8 of the $z \sim 2$ galaxies which also have H α line widths. The eight galaxies have H α velocity dispersions ranging from 60 to 150 km s $^{-1}$. There is no systematic difference in the velocity dispersion from the two lines, with $\langle \sigma_{\text{H}\alpha} \rangle = 95$ km s $^{-1}$, and $\langle \sigma_{[\text{O III}]}$ = 97 km s $^{-1}$. The individual values of σ usually agree well, and when they do not, contamination by sky lines, particularly in the H -band where we measure [O III], appears to be the source of the discrepancy. There is therefore no evidence that the use of different lines is a significant issue in the comparison of the two samples.

Another possible factor is the higher redshift of the LBGs. Surface brightness is a strong function of redshift, and it is possible that we are seeing only the brightest, most central regions of the LBGs compared with flux from a larger region of the $z \sim 2$ sample. If this is true, we might expect to observe less emission from the faint, low surface brightness portions of the galaxies at $z \sim 3$ than at $z \sim 2$; in other words, the $z \sim 3$ galaxies may appear smaller, beyond the expected scaling in size with redshift (e.g. Ferguson et al. 2004). We have measured the spatial extent of 18 of the [O III] emission lines, for comparison with the H α sizes; as in the $z \sim 2$ sample, most of the lines are spatially resolved, and $\langle r_{[\text{O III}]} \rangle = 0.6'' \simeq 4.5$ kpc. The mean value of $r_{[\text{O III}]}$ is slightly smaller than the mean H α spatial extent, for which we find $\langle r_{\text{H}\alpha} \rangle = 0.7'' \simeq 6$ kpc. This difference is almost identical to the mean size difference found between UV-bright galaxies at $z \sim 3$ and $z \sim 2.3$ by Ferguson et al. (2004), who find that galaxy radii scale with redshift approximately as the Hubble parameter $H^{-1}(z)$, in accordance with theoretical expectations. In our adopted cosmology, this scaling predicts that the $z \sim 3$ LBGs should have mean radii $\sim 70\%$ smaller than the $z \sim 2$ sample, entirely consistent with our observations. We therefore have reason to believe that the observed size differences reflect real differences between the two samples, rather than surface brightness effects.

The selection criteria for observation with NIRSPEC were somewhat different for the two samples. The $z \sim 3$ galaxies were chosen primarily because of their UV brightness, with additional objects selected because of their proximity to a QSO sightline. Unlike some of the observations of $z \sim 2$ galaxies, objects with bright or red near-IR magnitudes or colors were not favored. If such bright or red objects make up most of those with large line widths, this could be a plausible explanation for the differences. An examination of the list of $z \sim 2$ galaxies with $\sigma > 120$ km s $^{-1}$ shows that some of them were indeed selected for their bright or red near-IR properties, but an approximately equal number were not. The velocity dispersions of $z \sim 2$ galaxies along QSO sightlines, which should be representative of the sample as a whole, have the same distribution as that of the full $z \sim 2$ sample, indicating that the selection of near-IR bright or red objects is probably not responsible for the presence of objects with large velocity dispersions in the $z \sim 2$ sample and their absence among the LBGs.

Another possibility is that [O III] is more difficult to

detect in massive galaxies; with increasing metallicity, the ratio of [O III]/[O II] decreases, as does the ratio of the [O III] and [O II] lines to H β (or H α) for metallicities above $\sim 1/3 Z_{\odot}$. Thus the relative fluxes of H α and [O III] might be expected to depend strongly on metallicity and hence stellar mass (Tremonti et al. 2004; Erb et al. 2006a). Although uncertainties in flux calibration make the ratios uncertain, in our sample of $z \sim 2$ galaxies with both H α and [O III] measurements $F_{\text{H}\alpha}/F_{[\text{O III}]}$ ranges from ~ 0.5 to ~ 5 as stellar mass increases from $\sim 10^9$ to $\sim 10^{11}$ M $_{\odot}$, and [O III] is not detected for one of the most massive galaxies (we do detect H β for this object). We see that [O III] is weak in massive, relatively metal-rich galaxies, and this could contribute to the absence of objects with large line widths in the $z \sim 3$ NIRSPEC samples⁸. Not all of the objects with large velocity dispersions in the $z \sim 2$ sample have large stellar masses, however; $\sim 60\%$ of the objects with $M_{\text{dyn}} \gg M_{\star}$ have $\sigma > 130$ km s $^{-1}$, and these low stellar mass objects also have low metallicities which should result in strong [O III] lines. The absence of such galaxies from the $z \sim 3$ sample (there may be one; we have no near-IR photometry and no stellar mass estimate for the $z \sim 3$ galaxy with the largest velocity dispersion) is unlikely to be explained by selection effects, and probably indicates that low stellar mass galaxies with large line widths are rarer at $z \sim 3$ than at $z \sim 2$.

There are reasons to expect physical differences between the $z \sim 2$ and $z \sim 3$ samples. We have already noted that galaxies at $z \sim 3$ are seen to be more compact than those at $z \sim 2$, in agreement with expectations from hierarchical galaxy formation theory. An analysis of the correlation lengths of the LBGs and the $z \sim 2$ sample indicates that the $z \sim 2$ galaxies reside in halos ~ 3 times more massive than those hosting the LBGs (Adelberger et al. 2005b). The smaller dynamical masses of the $z \sim 3$ galaxies are in good agreement with this result. We conclude that the lower average velocity dispersion of the LBGs is not fully explained by selection effects, and that the differences in σ between the $z \sim 2$ and $z \sim 3$ samples are likely to indicate real differences in the typical masses of galaxies in the two samples.

5. SPATIALLY RESOLVED KINEMATICS

In our initial study of 16 H α spectra of $z \sim 2$ galaxies, nearly 40% of the sample showed spatially resolved and tilted emission lines (Erb et al. 2003). In the current, enlarged sample of 114 objects the fraction is much smaller, 14/114 or 12%; this is probably both because of exceptionally good conditions during our first observing run (we observed 6 of the 14 objects during this run) and simply because of small number statistics. Velocity shear may be caused by rotation, merging, or some combination of the two, and whether or not it is detected in a nebular emission line depends on the size, surface brightness and velocity structure of the object, its inclination, and the alignment of the slit with respect to the major axis. The seeing during the observations plays a crucial role as well, as Erb et al. (2004) show with repeated observations of the same object. Inclinations and

⁸ In principle we would still recognize $z \sim 3$ objects with large velocity dispersions via their broad H β lines, but in many cases H β is too weak for a reliable measurement

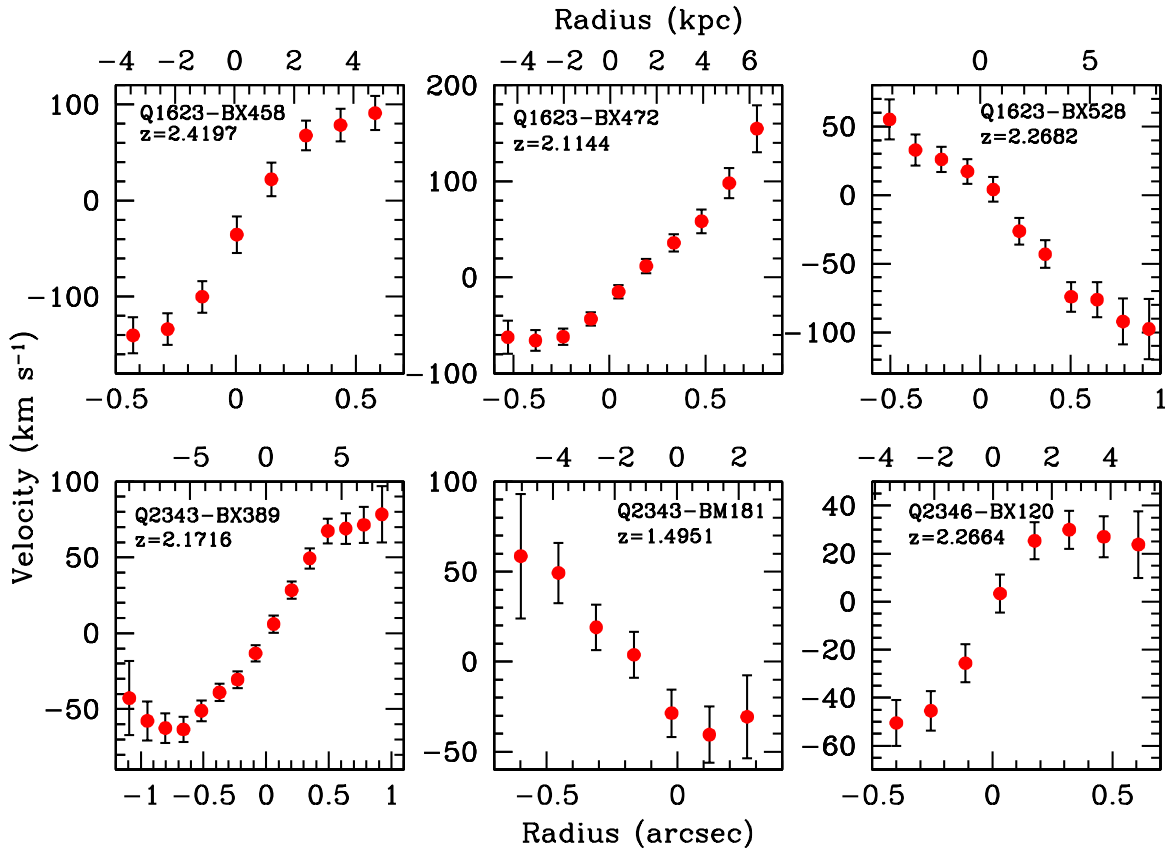


FIG. 14.— Observed velocity as a function of slit position for objects with spatially resolved and tilted $H\alpha$ emission lines. The seeing for these observations was $\sim 0.5''$, so the points shown are highly correlated, with approximately four points per resolution element. We plot one point per pixel to show the observed velocity field clearly, but the blurring of the seeing means that these diagrams do not represent the true velocity structure of the galaxies.

major axes are unknown for nearly all of our sample, as is the primary cause of the velocity shear, and therefore this fraction of 12% should be considered a lower limit to the fraction of rotating or merging objects in the $z \sim 2$ sample. The true fraction cannot be determined given the limitations imposed by the seeing.

In order for the tilt of an emission line to be considered significant, we required that the observed spatial extent be at least 1.5 times larger than the seeing disk, and that the peak-to-peak amplitude of the shear be at least four times larger than the typical velocity uncertainty. Five of the 14 objects with spatially resolved velocity shear have not been previously discussed (six are described by Erb et al. 2003, two by Erb et al. 2004, and one by Shapley et al. 2004). We plot the observed velocities with respect to systemic as a function of slit position for these five objects in Figure 14; we also include Q1623-BX528, the object discussed by Shapley et al. 2004, because such a diagram was not presented in that paper. These diagrams are constructed by stepping along the slit pixel by pixel, summing the flux of each pixel and its neighbor on either side to increase the S/N, and measuring the centroid in velocity at each position. We emphasize that these are not rotation curves of the variety plotted for local galaxies. The points are highly correlated because of the seeing ($\sim 0.5''$ for the observations presented here, thus there are ~ 4 points per resolution element; we plot one point per pixel to give a clear picture of the *observed* velocity field), and recovery of the true velocity structure requires a model for the struc-

ture of the object because of the degeneracies created by the seeing (see Law et al. 2006 for a demonstration). Although the physical scale corresponding to the angular scale is given at the top of each panel for reference, the implied mapping between physical radius and velocity is not a true representation of the structure of the object.

Although the seeing prevents us from determining the true velocity field of the objects, we can at least determine a lower limit on the amplitude of the velocity shear from the uncorrelated endpoints of each curve. We calculate the observed $v_c = (v_{\max} - v_{\min})/2$ for each object, where v_{\max} and v_{\min} are with respect to the systemic redshift. This estimate is almost certainly less than the true velocity shear because the inclinations of the galaxies are unknown, in most cases we have made no attempt to align the slit with the major axis, and the seeing effectively reduces the velocities at the endpoints by mixing the light from the edges of the galaxy with emission from higher surface brightness, lower velocity regions toward the center. Even under ideal conditions, the $H\alpha$ emission may not trace the true circular velocity; Lehnert & Heckman (1996) find that in local starburst galaxies the regions of high $H\alpha$ surface brightness sample only the inner, solid-body portion of the rotation curve. The observed values of v_c for the 14 objects with velocity shear are given in Table 4, and in the left panel of Figure 15 they are plotted against the velocity dispersion σ . The dotted line marks equal values; we see that $v_c \sim \sigma$ for most objects, though with considerable scatter.

The relationship between σ and the terminal velocity

V_c (we use v_c to refer to our observed velocity shear, and V_c to indicate the true circular velocity of a disk) has been quantified in samples of more local galaxies. Rix et al. (1997) find $\sigma \sim 0.6 V_c$, while Pizzella et al. (2005) find $V_c = 1.32 \sigma + 46$ for elliptical and high surface brightness disk galaxies, for $\sigma \gtrsim 50 \text{ km s}^{-1}$ and with velocities in km s^{-1} . It is clear that σ and v_c of the galaxies in our sample do not follow these distributions; instead we find a mean $\langle \sigma/v_c \rangle \sim 1.2$ (while it is not possible for V_c to be less than σ , in the limit as the galaxy becomes spatially unresolved the *observed* $v_c \rightarrow 0$, and $\sigma/v_c \rightarrow \infty$). Because our measurements of σ are less affected by the seeing, they are undoubtedly more reliable than our measurements of v_c . If we assume for the moment that our galaxies are rotating disks, we can use one of the local relations to predict V_c for our sample. If the $z \sim 2$ galaxies obey the relation of Pizzella et al. (2005), our measurements of v_c underestimate the true circular velocities by an average factor of ~ 2 , and the full $\text{H}\alpha$ sample has an average $\langle V_c \rangle \sim 190 \text{ km s}^{-1}$. We have already shown that a change in the seeing from $\sim 0.5''$ to $\sim 0.9''$ can reduce the observed v_c by a factor of ~ 2 while changing σ by less than 10% (Erb et al. 2004), so it is not unreasonable to assume that a change in resolution from $\sim 0.1''$ or better to $\sim 0.5''$ might have a similar effect. Deep observations of these objects at high angular resolution will be required to obtain a true measure of V_c .

Next we ask whether or not the galaxies which display velocity shear are different from the rest of the galaxies in any significant way. Figure 15 shows that galaxies with shear span nearly the full range in velocity dispersion; the mean value of σ for the galaxies with shear is 119 km s^{-1} , while the mean σ of galaxies without shear is 120 km s^{-1} . There is mild evidence that galaxies with shear tend to be older; the median age of the galaxies with shear is 1434 Myr, compared to 509 Myr for the galaxies without shear. The galaxies with shear also have slightly higher stellar masses, with a median of $4.4 \times 10^{10} M_\odot$ compared to 1.8×10^{10} for those without shear. A larger sample of galaxies with shear, and more uniform observing conditions, are required to determine whether or not these differences are significant. Assuming for the moment that they are, they may suggest that the rotation of mature, dynamically relaxed galaxies is a more important contribution to our observed shear than merging, which should not have a preference for older, more massive galaxies.

Nothing in the data is inconsistent with ordered rotation as the primary cause of the observed shear. With this in mind we draw attention to the position-velocity diagram of Q2343-BX389, shown in the lower left panel of Figure 14, which appears to turn over or flatten at both ends in the manner of locally observed rotation curves. This is one of several objects from the $z \sim 2$ sample recently observed with SINFONI, the near-IR integral field spectrograph on the VLT (Förster Schreiber et al. 2006). The SINFONI position-velocity diagram also shows evidence for flattening, but at higher velocities; the velocity difference is probably due to the $\sim 50^\circ$ misalignment of the NIRSPEC slit with the kinematic major axis and the deeper SINFONI integration which reveals flux at larger radii. Several but not all of the galaxies observed with SINFONI show signatures of rotating disks, and the role

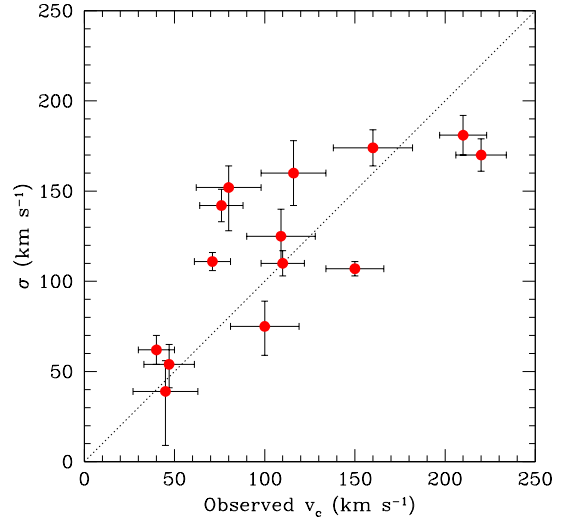


FIG. 15.— A comparison of the velocity dispersion σ and the observed velocity shear $v_c = (v_{\max} - v_{\min})/2$ for the 14 objects with tilted lines. The dotted line shows equal values. We find $\langle \sigma/v_c \rangle = 1.2$.

of merging in $z \sim 2$ galaxies still remains unclear. Given its expected importance at high redshift it is likely that it makes some contribution to our observed velocities. Improved disentangling of these effects must await high angular resolution spectroscopy with the aid of adaptive optics; such instruments will be able to map the velocity fields of high redshift galaxies at a resolution impossible with our current data (Law et al. 2006).

6. GAS AND BARYONIC MASSES

We have used the stellar and dynamical masses determined above to infer that the galaxies in our sample have significant gas fractions. It would be highly desirable to test this directly, for example with CO measurements, but such data would require extremely long integration times with current technology, making the assembly of a large sample of gas masses impossible. We can, however, exploit the correlation between star formation and gas density to obtain an estimate of the gas masses. In star-forming galaxies in the local universe, the surface densities of star formation and gas are observed to follow a Schmidt (1959) law, $\Sigma_{\text{SFR}} = A \Sigma_{\text{gas}}^N$, over more than six orders of magnitude in Σ_{SFR} (Kennicutt 1998). This empirical relation is usually explained by a model in which the SFR scales with density-dependent gravitational instabilities in the gas. The correlation has not yet been tested at high redshift because of the lack of measurements of gas masses, although the one well-studied example, the lensed $z = 2.7$ LBG MS1512-cB58, appears to be consistent with the local Schmidt law (Baker et al. 2004). Assuming that the galaxies in our sample obey such a law, we can use the SFRs and the galaxy sizes $r_{\text{H}\alpha}$ measured from the spatial extent of the $\text{H}\alpha$ emission to compute their star formation densities, and thus estimate their gas densities and masses. We use the global Schmidt law of Kennicutt (1998):

$$\Sigma_{\text{SFR}} = 2.5 \times 10^{-4} \left(\frac{\Sigma_{\text{gas}}}{1 M_\odot \text{ pc}^{-2}} \right)^{1.4} M_\odot \text{ yr}^{-1} \text{ kpc}^{-2} \quad (3)$$

in combination with the conversion from $H\alpha$ luminosity to SFR from the same paper,

$$\text{SFR} (M_{\odot} \text{ yr}^{-1}) = \frac{L(H\alpha)}{1.26 \times 10^{41} \text{ erg s}^{-1}} \quad (4)$$

to create an IMF-independent relation between our observed $H\alpha$ luminosity per unit area and the gas surface density

$$\Sigma_{\text{gas}} = 1.6 \times 10^{-27} \left(\frac{\Sigma_{H\alpha}}{\text{erg s}^{-1} \text{ kpc}^{-2}} \right)^{0.71} M_{\odot} \text{ pc}^{-2}. \quad (5)$$

The radii used by Kennicutt (1998) to compute surface densities approximately coincide with the edge of the galaxies' $H\alpha$ -emitting disks; for our surface densities, we take an area equal to the square of the FWHM of the (continuum-subtracted when necessary) $H\alpha$ emission ($r_{H\alpha}$ in Table 4). For $L(H\alpha)$ we use the extinction-corrected $H\alpha$ luminosity, incorporating the factor of 2 aperture correction discussed by Erb et al. (2006b). We then take $M_{\text{gas}} = \Sigma_{\text{gas}} r_{H\alpha}^2$ as an estimate of the cold gas mass associated with star formation, and calculate the gas fraction $\mu \equiv M_{\text{gas}} / (M_{\text{gas}} + M_{\star})$. The removal of the IMF dependence from the Schmidt law (which assumes a Salpeter IMF in the conversion from $H\alpha$ luminosity to SFR) facilitates comparison between gas, dynamical and stellar masses, as we discuss below. It is likely to be difficult to measure the objects' sizes with accuracy, given their often clumpy UV continuum morphologies as seen in high resolution images (e.g. Erb et al. 2003, 2004); the $H\alpha$ morphology is likely to be complicated as well. As noted in §4, the object sizes have typical uncertainties of $\sim 30\%$, and the corrected $H\alpha$ fluxes of the objects may be uncertain by up to a factor of ~ 2 ; therefore the gas masses of individual objects are uncertain by a factor of ~ 3 , and the typical fractional uncertainty in μ is $\sim 50\%$. Systematic uncertainties due to the scatter in the Schmidt law itself (0.3 dex) are an additional source of error. We focus here on overall trends, which depend on large numbers of objects and so are better determined than the parameters of individual galaxies; for example, the error in the mean gas fraction of a subsample of ~ 15 objects is 15% or less.

The mean inferred gas mass is $\langle M_{\text{gas}} \rangle = 2.1 \pm 0.1 \times 10^{10} M_{\odot}$, slightly lower than the mean stellar mass of $\langle M_{\star} \rangle = 3.6 \pm 0.4 \times 10^{10} M_{\odot}$. The distributions of the two masses are shown in the histograms in the upper left panel of Figure 16, where the narrower blue histogram shows the gas masses and the broader red histogram shows the stellar masses. The range of inferred gas masses is clearly smaller than the range of stellar masses; this is because the dispersions in star formation rate and size are smaller than the more than two orders of magnitude variation we see in stellar mass. The two masses are plotted against each other in the upper right panel of Figure 16, where it is apparent that the $M_{\text{dyn}}/M_{\star} > 10$ objects (open diamonds) have large inferred gas masses, and are exceptions to a general trend of increasing gas mass with increasing stellar mass. The absence of points in the lower left corner of this plot is probably a selection effect, as low mass galaxies with low star formation rates are unlikely to be detected in our K -band images (they may fall below our $\mathcal{R} < 25.5$ magnitude limit for selection as well), and we are also less likely to detect $H\alpha$ emission in K -faint

objects. We next plot the gas fraction μ vs. stellar mass in the lower left panel of Figure 16 and μ vs. age in the lower right. The trends of decreasing gas fraction with increasing stellar mass and age are strong, supporting our hypothesis that the $M_{\text{dyn}} \gg M_{\star}$ objects are young starbursts with high gas fractions (low mass galaxies with low gas fractions may exist, but are probably too faint to be detected by our survey). Local galaxies with low stellar masses are also observed to have higher gas fractions (McGaugh & de Blok 1997; Bell & de Jong 2000).

Other studies of galaxies at high and low redshift may provide additional insight into these results. Reddy et al. (2006) have recently used 24 μm data from the Spitzer Space Telescope to infer the bolometric luminosities of both optically-selected galaxies similar to those considered here and near-IR selected objects (Daddi et al. 2004; Franx et al. 2003). They assess the relationship between gas fraction and stellar mass, finding a similar strong trend which extends to massive, nearly passively evolving galaxies with low gas fractions that are not selected by our UV criteria. They also consider the dust-to-gas ratio of local and high redshift galaxies, finding that at a given bolometric luminosity galaxies at $z \sim 2$ are ~ 10 times less obscured by dust than local galaxies. Thus we infer that FIR emission is likely to be weaker in high redshift gas-rich galaxies than in their low redshift counterparts with similar bolometric luminosities. Galaxies that are detected at 850 μm have so far provided the best candidates for direct detection of gas in high redshift galaxies; Greve et al. (2005) use CO measurements to estimate the gas masses of five submillimeter galaxies at $z = 1-3.5$, finding a median molecular gas mass of $3.0 \times 10^{10} M_{\odot}$ within a typical radius of ~ 2 kpc. This is only slightly higher than the typical gas masses we infer from the Schmidt law, implying that the largest gas masses we infer may be testable with current technology. Though the gas masses of the submm galaxies appear to be similar to those we find here, the factor of ~ 3 smaller sizes of the submm galaxies imply a gas surface density an order of magnitude higher than the average value of our sample. Such comparisons must be viewed with caution, of course, given the very different methods of inferring the gas content and sizes of the two samples; it is possible that a more direct measurement of the molecular gas distribution of the current sample would reveal smaller emitting regions and higher gas surface densities.

We can now compare the estimated baryonic masses $M_{\text{bar}} = M_{\text{gas}} + M_{\star}$ with the dynamical masses in Figure 17, to see if the addition of the inferred gas mass improves the agreement between stellar and dynamical mass. We use the same axes as Figure 7 to facilitate comparison, and again mark the line of equal masses (dashed line) and a factor of ~ 6 difference between the two masses (dotted lines). The agreement between the masses is greatly improved with the addition of the gas; there is a significant correlation (4σ , with probability $P = 8 \times 10^{-5}$ that the data are uncorrelated), and the masses are within a factor of 3 for 85% of the sample (objects with limits on σ are not included, though most of these are consistent with the rest of the data, and those that are inconsistent are highly uncertain). After excluding AGN (open circles), we find $\langle M_{\text{gas}} + M_{\star} \rangle = 5.8 \pm 0.6 \times 10^{10} M_{\odot}$; the mean dynamical

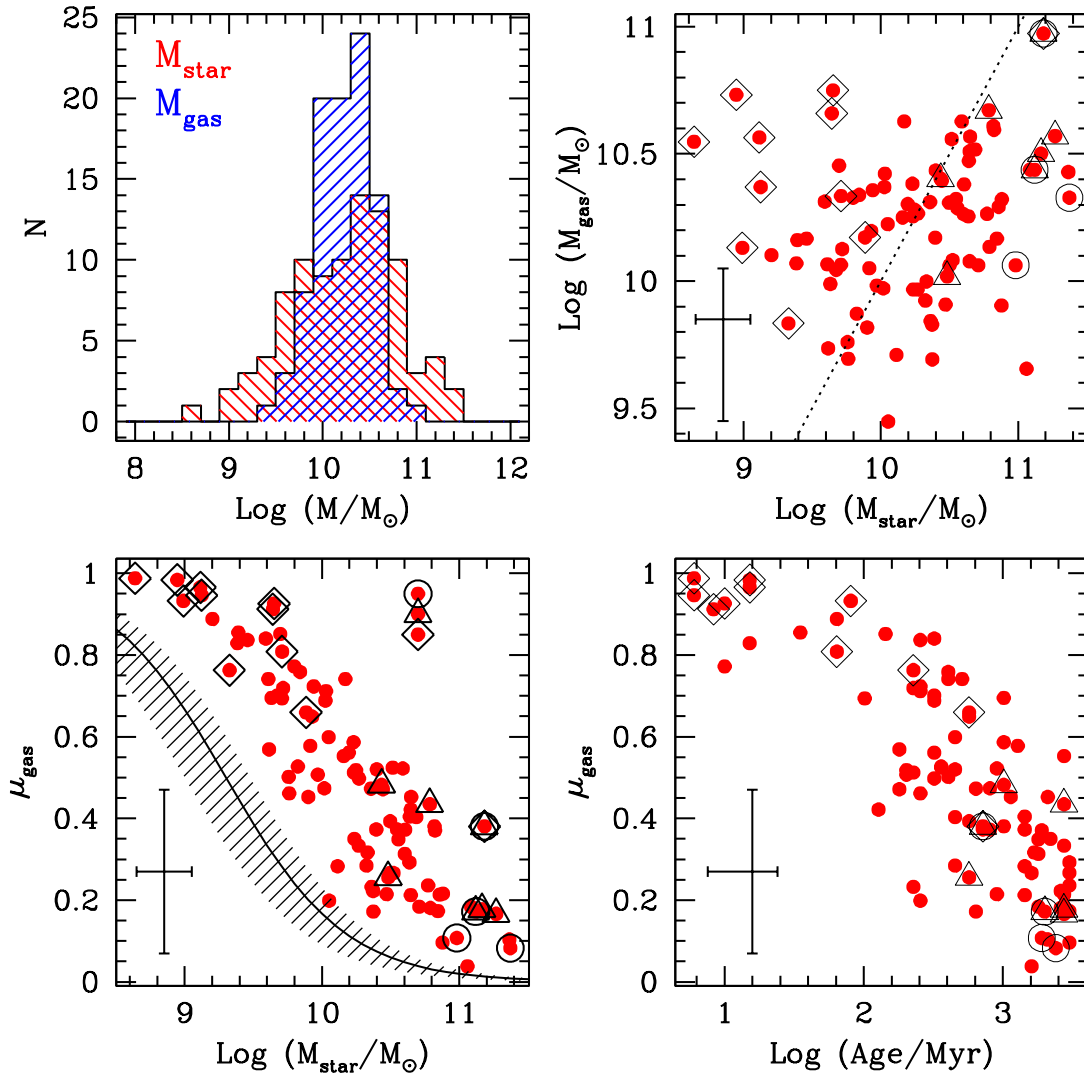


FIG. 16.— The relation of the gas mass inferred from the Schmidt law to the stellar population parameters. Upper left: Histograms of the gas (blue) and stellar (red) masses, showing that the range in stellar mass is significantly broader than the range in gas mass. Upper right: Gas mass vs. stellar mass. Gas masses are relatively constant across the sample, but when the galaxies with $M_{\text{dyn}}/M_\star > 10$ are not considered we see an increase in gas mass with stellar mass. Lower panels: The gas fraction strongly decreases with increasing stellar mass (left) and age (right). The solid line and accompanying shaded region in the lower left panel show the minimum detectable gas fraction set by our $\text{H}\alpha$ flux detection limit, for the mean (solid line) and range (shaded region) of sizes observed. Symbols are as in Figure 7, and the error bars in the corner of each plot show typical uncertainties.

mass $\langle M_{\text{dyn}} \rangle = 7.1 \pm 0.7 \times 10^{10} M_\odot$ is 1.2 times higher. There are only two objects for which $M_{\text{dyn}}/M_{\text{bar}} > 10$; these are the AGN Q1700-MD94 (upper right), and the galaxy Q1623-BX376, which has an anomalously large velocity dispersion that may be influenced by its complicated spatial structure (Erb et al. 2003).

Although the estimates of gas, stellar and dynamical masses considered here carry significant uncertainties, we emphasize that they are obtained from independent quantities ($\text{H}\alpha$ luminosity and size, multi-wavelength photometry, and line width respectively). Together they provide a remarkably coherent scenario in which relatively massive ($M_{\text{gas}} + M_\star \gtrsim 10^{10} M_\odot$, and $M_{\text{halo}} \sim 10^{12} M_\odot$; Adelberger et al. 2005b) star-forming galaxies have high gas fractions which decrease with age. The observed variation of metallicity across the sample also supports this model, as we describe separately (Erb et al. 2006a).

In this scenario, the stellar mass of a galaxy depends strongly on its evolutionary state, as well as on its total mass. The lowest stellar mass galaxies in the sample have low stellar masses because they are young and have converted or expelled only a small fraction of their gas; such objects have stellar masses $\gtrsim 100$ times lower than the most massive galaxies in the sample, while their inferred baryonic and dynamical masses are only $\lesssim 30$ times lower than those of the most massive galaxies.

7. CONCLUSIONS AND DISCUSSION

The goals of this paper have been to examine the kinematic properties of star-forming galaxies at $z \sim 2$ as revealed by their $\text{H}\alpha$ spectra; to compare their dynamical masses with stellar masses determined from population synthesis modeling; to look for trends between kinematic and stellar population properties; and to estimate the

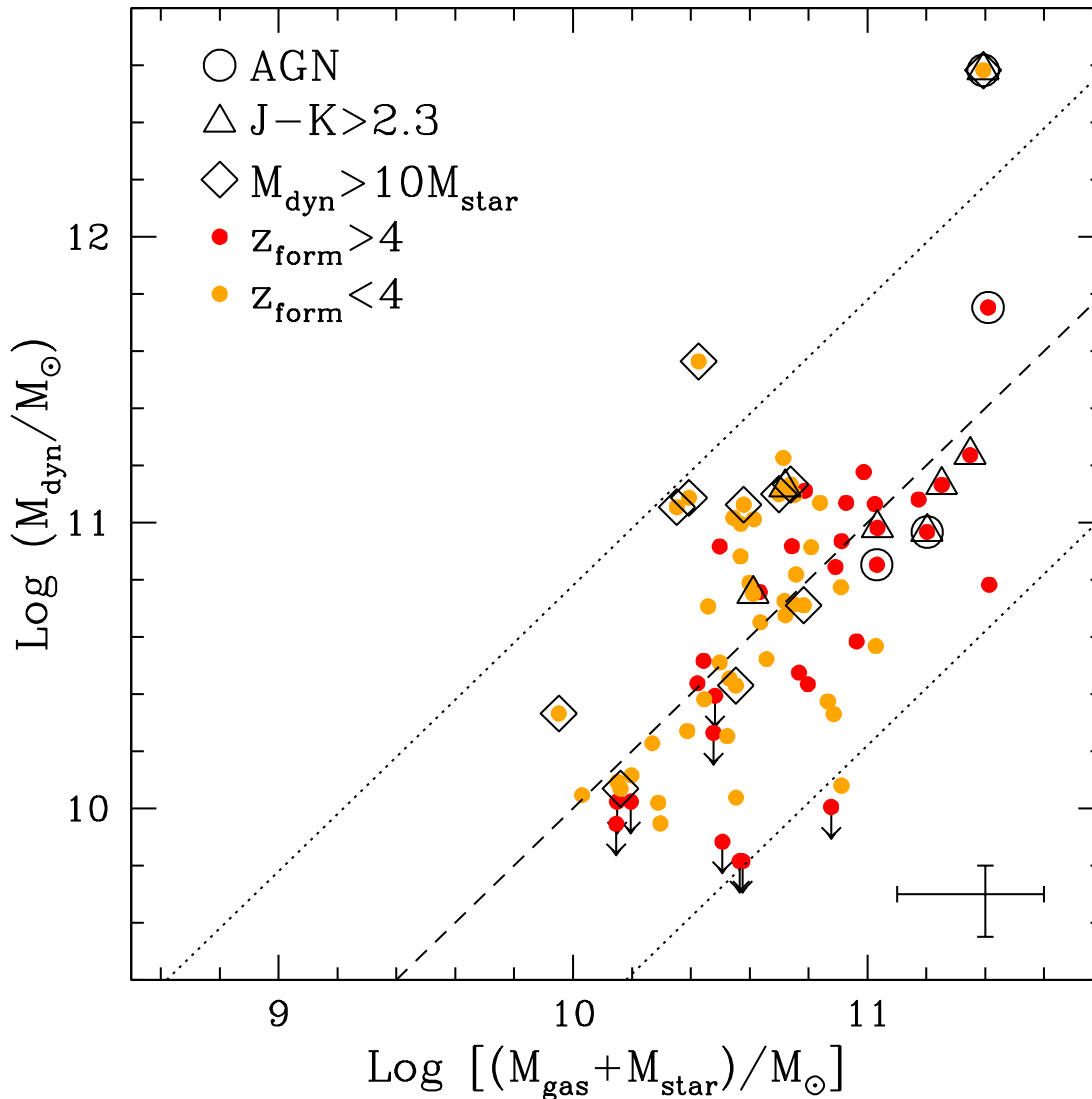


FIG. 17.— The combined gas and stellar mass $M_{\text{gas}} + M_{\star}$ vs. dynamical mass M_{dyn} ; compare Figure 7. The dashed line shows equal masses, and the dotted lines show a factor of ~ 6 difference between the masses. The correlation is significant at the 4σ level, and the masses of 85% of the objects agree to within a factor of three. Neglecting AGN, the average dynamical mass is 1.2 times larger than the average baryonic mass. Symbols are as in Figure 7, with the addition that galaxies with inferred formation redshifts (discussed in §7) $z_{\text{form}} > 4$ are shown in red and those with $z_{\text{form}} < 4$ are shown in orange. Typical uncertainties are shown by the error bars in the lower left corner, which for dynamical masses include only measurement errors in $r_{\text{H}\alpha}$ and σ . Uncertainties in dynamical masses are dominated by the unknown factors in the mass model as discussed in the text; the dotted lines indicate approximate uncertainties in the mass comparison including this additional source of error.

stellar and gas content of the galaxies. Our main conclusions are as follows:

1. The sample has a mean $\text{H}\alpha$ velocity dispersion $\langle \sigma \rangle = 101 \pm 5 \text{ km s}^{-1}$, excluding AGN. From σ and the spatial extent of the $\text{H}\alpha$ emission we estimate dynamical masses, finding $\langle M_{\text{dyn}} \rangle = 7.1 \pm 0.7 \times 10^{10} M_{\odot}$, again excluding AGN. Stellar and dynamical masses agree to within a factor of ~ 6 for most objects, consistent with observational and systematic uncertainties. The masses are correlated with 2.5σ significance. However, 15% of the galaxies have $M_{\text{dyn}} > 10 \times M_{\star}$; these objects have low stellar masses, young ages and tend to have high $\text{H}\alpha$ equivalent widths, suggesting that they are young galaxies with large gas fractions.

2. We combine our $\text{H}\alpha$ results with LBGs at $z \sim 3$ and other samples from the literature, and find that rest-

frame optical luminosity (corrected for extinction) and velocity dispersion are correlated with 4σ significance. The large scatter prevents a robust determination of the slope, but it is not inconsistent with the local relation $L \propto \sigma^4$. The high redshift galaxies have much higher luminosities at a given velocity dispersion than would be predicted by the local Faber-Jackson relation. The observed correlation and its accompanying large scatter suggest that the processes which produce the L - σ correlation in the local universe are underway at $z \sim 2$ -3.

3. A comparison of the $\text{H}\alpha$ sample with a similarly rest-frame UV-selected sample of Lyman break galaxies at $z \sim 3$ shows that the average velocity dispersion is $\sim 30\%$ larger at $z \sim 2$ than at $z \sim 3$, and the average dynamical mass of the $z \sim 2$ galaxies is ~ 2 times larger than that of the $z \sim 3$ LBGs. This difference proba-

bly reflects real differences in the average masses of the galaxies at $z \sim 2$ and $z \sim 3$.

4. Fourteen of the 114 galaxies with H α spectra, or 12%, have spatially resolved and tilted emission lines. On average, the observed amplitude of the velocity shear v_c is approximately equal to the velocity dispersion σ . If the galaxies are rotating disks and follow the local relations between the true circular velocity V_c and σ , our observations underestimate V_c by an average factor of ~ 2 , and the galaxies have $\langle V_c \rangle \sim 190 \text{ km s}^{-1}$. However, other factors including galaxy-galaxy mergers, slit position angle, and the seeing FWHM are significant sources of uncertainty in v_c .

5. Using the empirical correlation between star formation rate per unit area and gas surface density, we estimate gas masses and gas fractions for the galaxies in the sample. The mean gas fraction is $\sim 50\%$, and the gas fraction strongly decreases with increasing stellar mass and age. The combined mass in gas and stars is significantly better correlated with the dynamical mass than is the stellar mass alone. The sample spans a much wider range in stellar mass than dynamical mass (or inferred baryonic mass), indicating that there is considerable dispersion in the fraction of gas that has been converted to stars by $z \sim 2$.

These differing ranges in stellar and baryonic mass imply that galaxies of similar total masses began forming stars at different times, and that at a given redshift galaxies with a wide variety of total masses have just begun forming stars. For $\sim 70\%$ of the galaxies in the H α sample, the best-fit ages imply formation redshifts $2 \lesssim z_{\text{form}} \lesssim 4$; most of these galaxies have baryonic masses between $\sim 10^{10}$ and $\sim 10^{11} M_{\odot}$. The remaining $\sim 30\%$ have $z_{\text{form}} > 4$ (including the 15% of the sample which have best-fit ages equal to the age of the universe); these galaxies have $10^{10.4} \lesssim M_{\text{bar}} \lesssim 10^{11.4} M_{\odot}$. M_{bar} and z_{form} are strongly correlated across the full sample, with 5.4σ significance, while those with $2 \lesssim z_{\text{form}} \lesssim 4$ are correlated with 2.2σ significance and there is no correlation between M_{bar} and z_{form} within the $z_{\text{form}} > 4$ group. The two groups are shown in Figure 17, where galaxies with $z_{\text{form}} > 4$ are shown by red points and galaxies with $z_{\text{form}} < 4$ are plotted in orange. Galaxies with $M_{\text{bar}} \lesssim 10^{11} M_{\odot}$ fall in both groups. These results are not unexpected, since total mass is not the only factor which determines when a galaxy begins to form stars; large scale environment and interactions with other galaxies are also significant. Galaxies in dense environments will cross the critical density threshold for

collapse earlier, and should therefore begin forming stars at earlier times. One of the fields in the present survey contains a significant overdensity of galaxies at $z = 2.3$, and Steidel et al. (2005) show that galaxies within the overdensity are significantly older than average. It is also expected that mergers will trigger significant star formation events; the merger-based numerical simulations of Springel et al. (2005, and references therein) are successful in reproducing many properties of galaxies. We cannot yet identify the likely triggers for star formation for galaxies on an individual basis, however; detailed morphological analysis and an improved quantification of the galaxies' environments will be useful in this regard.

Because of uncertainties in the sizes and velocity distributions of the $z \sim 2$ galaxies, the dynamical masses presented here have much room for improvement. These improvements will require deep observations of a large sample of objects, and in many cases high angular resolution will be needed in order to discriminate between plausible models of the velocity field. Near-IR multi-object and integral field spectrographs, especially with adaptive optics, will make such observations feasible, and we anticipate that the galaxies presented here will be a useful sample from which to select targets for such observations. These kinematic measurements will provide otherwise unobtainable insights about the prevalence of mergers at high redshift and the growth of massive disk galaxies. We also anticipate studies at longer wavelengths which will improve our understanding of the galaxies' gas masses. All of these results will lead to a more refined picture of the assembly of mass at high redshift.

We thank Andrew Blain, Jonathan Bird, David Kaplan and Shri Kulkarni for obtaining near-IR images of some of our targets; the staffs of the Keck and Palomar observatories for their assistance with the observations; and the anonymous referee for a thoroughly helpful report that significantly improved the paper. CCS, DKE and NAR have been supported by grant AST03-07263 from the US National Science Foundation and by the David and Lucile Packard Foundation. AES acknowledges support from the Miller Institute for Basic Research in Science, and KLA from the Carnegie Institution of Washington. Finally, we wish to extend special thanks to those of Hawaiian ancestry on whose sacred mountain we are privileged to be guests. Without their generous hospitality, most of the observations presented herein would not have been possible.

REFERENCES

- Adelberger, K. L., Shapley, A. E., Steidel, C. C., Pettini, M., Erb, D. K., & Reddy, N. A. 2005a, *ApJ*, 629, 636
 Adelberger, K. L., Steidel, C. C., Pettini, M., Shapley, A. E., Reddy, N. A., & Erb, D. K. 2005b, *ApJ*, 619, 697
 Baker, A. J., Tacconi, L. J., Genzel, R., Lehnert, M. D., & Lutz, D. 2004, *ApJ*, 604, 125
 Barmby, P., Huang, J.-S., Fazio, G. G., Surace, J. A., Arendt, R. G., Hora, J. L., Pahre, M. A., Adelberger, K. L., Eisenhardt, P., Erb, D. K., Pettini, M., Reach, W. T., Reddy, N. A., Shapley, A. E., Steidel, C. C., Stern, D., Wang, Z., & Willner, S. P. 2004, *ApJS*, 154, 97
 Begelman, M. C. & Nath, B. B. 2005, *MNRAS*, 361, 1387
 Bell, E. F. & de Jong, R. S. 2000, *MNRAS*, 312, 497
 Bell, E. F., McIntosh, D. H., Katz, N., & Weinberg, M. D. 2003, *ApJS*, 149, 289
 Bell, E. F., Papovich, C., Wolf, C., Le Floch, E., Caldwell, J. A. R., Barden, M., Egami, E., McIntosh, D. H., Meisenheimer, K., Pérez-González, P. G., Rieke, G. H., Rieke, M. J., Rigby, J. R., & Rix, H.-W. 2005, *ApJ*, 625, 23
 Bernardi, M., Sheth, R. K., Annis, J., Burles, S., Eisenstein, D. J., Finkbeiner, D. P., Hogg, D. W., Lupton, R. H., Schlegel, D. J., SubbaRao, M., Bahcall, N. A., Blakeslee, J. P., Brinkmann, J., Castander, F. J., Connolly, A. J., Csabai, I., Doi, M., Fukugita, M., Frieman, J., Heckman, T., Hennessy, G. S., Ivezić, Ž., Knapp, G. R., Lamb, D. Q., McKay, T., Munn, J. A., Nichol, R., Okamura, S., Schneider, D. P., Thakar, A. R., & York, D. G. 2003, *AJ*, 125, 1849
 Brinchmann, J. & Ellis, R. S. 2000, *ApJ*, 536, L77
 Bruzual, G. & Charlot, S. 2003, *MNRAS*, 344, 1000

- Calzetti, D., Armus, L., Bohlin, R. C., Kinney, A. L., Koornneef, J., & Storchi-Bergmann, T. 2000, *ApJ*, 533, 682
- Cardone, V. F. & Sereno, M. 2005, *A&A*, 438, 545
- Chabrier, G. 2003, *PASP*, 115, 763
- Cimatti, A., Daddi, E., Mignoli, M., Pozzetti, L., Renzini, A., Zamorani, G., Broadhurst, T., Fontana, A., Saracco, P., Poli, F., Cristiani, S., D'Odorico, S., Giallongo, E., Gilmozzi, R., & Menci, N. 2002, *A&A*, 381, L68
- Colina, L., Arribas, S., & Monreal-Ibero, A. 2005, *ApJ*, 621, 725
- Courteau, S. 1997, *AJ*, 114, 2402
- Daddi, E., Cimatti, A., Renzini, A., Fontana, A., Mignoli, M., Pozzetti, L., Tozzi, P., & Zamorani, G. 2004, *ApJ*, 617, 746
- Davé, R., Finlator, K., Hernquist, L., Katz, N., Kereš, D., Papovich, C., & Weinberg, D. H. 2005, *ArXiv Astrophysics e-prints*, astro-ph/0510625
- Di Matteo, T., Croft, R. A. C., Springel, V., & Hernquist, L. 2003, *ApJ*, 593, 56
- Di Matteo, T., Springel, V., & Hernquist, L. 2005, *Nature*, 433, 604
- Dickinson, M., Papovich, C., Ferguson, H. C., & Budavári, T. 2003, *ApJ*, 587, 25
- Erb, D. K., Shapley, A. E., Pettini, M., Steidel, C. C., Reddy, N. A., & Adelberger, K. L. 2006a, *ApJ*, in press, astro-ph/0602473
- Erb, D. K., Shapley, A. E., Steidel, C. C., Pettini, M., Adelberger, K. L., Hunt, M. P., Moorwood, A. F. M., & Cuby, J. 2003, *ApJ*, 591, 101
- Erb, D. K., Steidel, C. C., Shapley, A. E., Pettini, M., & Adelberger, K. L. 2004, *ApJ*, 612, 122
- Erb, D. K., Steidel, C. C., Shapley, A. E., Pettini, M., Reddy, N. A., & Adelberger, K. L. 2006b, *ApJ*, submitted
- Förster Schreiber, N. M., Genzel, R., Lehnert, M. D., Erb, D. K., Shapley, A. E., Steidel, C. C., Bouché, N., Davies, R., Lutz, D., Nesvadba, N., Tacconi, L. J., Verma, A., Eisenhauer, F., Gilbert, A., & Gillessen, S. 2006, *ApJ*, in press, astro-ph/0603559
- Förster Schreiber, N. M., van Dokkum, P. G., Franx, M., Labbé, I., Rudnick, G., Daddi, E., Illingworth, G. D., Kriek, M., Moorwood, A. F. M., Rix, H.-W., Röttgering, H., Trujillo, I., van der Werf, P., van Starckenburg, L., & Wuyts, S. 2004, *ApJ*, 616, 40
- Faber, S. M. & Jackson, R. E. 1976, *ApJ*, 204, 668
- Fan, X. et al. 2001, *AJ*, 121, 54
- Ferguson, H. C., Dickinson, M., Giavalisco, M., Kretchmer, C., Ravindranath, S., Idzi, R., Taylor, E., Conselice, C. J., Fall, S. M., Gardner, J. P., Livio, M., Madau, P., Moustakas, L. A., Papovich, C. M., Somerville, R. S., Spinrad, H., & Stern, D. 2004, *ApJ*, 600, L107
- Ferrarese, L. & Merritt, D. 2000, *ApJ*, 539, L9
- Franx, M., Labbé, I., Rudnick, G., van Dokkum, P. G., Daddi, E., Förster Schreiber, N. M., Moorwood, A., Rix, H., Röttgering, H., van der Werf, P., & van Starckenburg, L. 2003, *ApJ*, 587, L79
- Gebhardt, K., Bender, R., Bower, G., Dressler, A., Faber, S. M., Filippenko, A. V., Green, R., Grillmair, C., Ho, L. C., Kormendy, J., Lauer, T. R., Magorrian, J., Pinkney, J., Richstone, D., & Tremaine, S. 2000, *ApJ*, 539, L13
- Greve, T. R., Bertoldi, F., Smail, I., Neri, R., Chapman, S. C., Blain, A. W., Ivison, R. J., Genzel, R., Omont, A., Cox, P., Tacconi, L., & Kneib, J.-P. 2005, *MNRAS*, 359, 1165
- Heavens, A., Panter, B., Jimenez, R., & Dunlop, J. 2004, *Nature*, 428, 625
- Juneau, S., Glazebrook, K., Crampton, D., McCarthy, P. J., Savaglio, S., Abraham, R., Carlberg, R. G., Chen, H., Le Borgne, D., Marzke, R. O., Roth, K., Jørgensen, I., Hook, I., & Murowinski, R. 2005, *ApJ*, 619, L135
- Kennicutt, R. C. 1998, *ApJ*, 498, 541
- Kobulnicky, H. A. & Gebhardt, K. 2000, *AJ*, 119, 1608
- Kroupa, P. 2001, *MNRAS*, 322, 231
- Law, D. R., Steidel, C. C., & Erb, D. K. 2006, *AJ*, 131, 70
- Lehnert, M. D. & Heckman, T. M. 1996, *ApJ*, 472, 546
- Magorrian, J., Tremaine, S., Richstone, D., Bender, R., Bower, G., Dressler, A., Faber, S. M., Gebhardt, K., Green, R., Grillmair, C., Kormendy, J., & Lauer, T. 1998, *AJ*, 115, 2285
- Marconi, A. & Hunt, L. K. 2003, *ApJ*, 589, L21
- Martin, C. L. & Kennicutt, R. C. 2001, *ApJ*, 555, 301
- Matthews, K. & Soifer, B. T. 1994, in *ASSL Vol. 190: Astronomy with Arrays, The Next Generation*, 239
- McGaugh, S. S. & de Blok, W. J. G. 1997, *ApJ*, 481, 689
- McLean, I. S., Becklin, E. E., Bendiksen, O., Brims, G., Canfield, J., Figer, D. F., Graham, J. R., Hare, J., Lacayanga, F., Larkin, J. E., Larson, S. B., Levenson, N., Magnone, N., Teplitz, H., & Wong, W. 1998, in *Proc. SPIE Vol. 3354*, p. 566-578, *Infrared Astronomical Instrumentation*, Albert M. Fowler; Ed., Vol. 3354, 566-578
- Mo, H. J. & Mao, S. 2004, *MNRAS*, 353, 829
- Murray, N., Quataert, E., & Thompson, T. A. 2005, *ApJ*, 618, 569
- Padmanabhan, N., Seljak, U., Strauss, M. A., Blanton, M. R., Kauffmann, G., Schlegel, D. J., Tremonti, C., Bahcall, N. A., Bernardi, M., Brinkmann, J., Fukugita, M., & Ivezić, Z. 2004, *New Astronomy*, 9, 329
- Papovich, C., Dickinson, M., & Ferguson, H. C. 2001, *ApJ*, 559, 620
- Pettini, M., Shapley, A. E., Steidel, C. C., Cuby, J., Dickinson, M., Moorwood, A. F. M., Adelberger, K. L., & Giavalisco, M. 2001, *ApJ*, 554, 981
- Pizzella, A., Corsini, E. M., Dalla Bontà, E., Sarzi, M., Coccato, L., & Bertola, F. 2005, *ApJ*, 631, 785
- Reddy, N. A., Erb, D. K., Steidel, C. C., Shapley, A. E., Adelberger, K. L., & Pettini, M. 2005, *ApJ*, 633, 748
- Reddy, N. A., Steidel, C. C., Fadda, D., Yan, L., Pettini, M., Shapley, A. E., Erb, D. K., & Adelberger, K. L. 2006, *ApJ*, in press, astro-ph/0602596
- Renzini, A. 2005, in *IMF@50: The Initial Mass Function, 50 Years Later*, in press, astro-ph/0410295
- Rix, H., Guhathakurta, P., Colless, M., & Ing, K. 1997, *MNRAS*, 285, 779
- Robertson, B., Hernquist, L., Cox, T. J., Di Matteo, T., Hopkins, P. F., Martini, P., & Springel, V. 2005, *ApJ*, submitted, astro-ph/0506038
- Rudnick, G., Rix, H.-W., Franx, M., Labbé, I., Blanton, M., Daddi, E., Förster Schreiber, N. M., Moorwood, A., Röttgering, H., Trujillo, I., van de Wel, A., van der Werf, P., van Dokkum, P. G., & van Starckenburg, L. 2003, *ApJ*, 599, 847
- Salpeter, E. E. 1955, *ApJ*, 121, 161
- Schmidt, M. 1959, *ApJ*, 129, 243
- Shapley, A. E., Erb, D. K., Pettini, M., Steidel, C. C., & Adelberger, K. L. 2004, *ApJ*, 612, 108
- Shapley, A. E., Steidel, C. C., Adelberger, K. L., Dickinson, M., Giavalisco, M., & Pettini, M. 2001, *ApJ*, 562, 95
- Shapley, A. E., Steidel, C. C., Erb, D. K., Reddy, N. A., Adelberger, K. L., Pettini, M., Barnby, P., & Huang, J. 2005, *ApJ*, 626, 698
- Spergel, D. N., Verde, L., Peiris, H. V., Komatsu, E., Nolte, M. R., Bennett, C. L., Halpern, M., Hinshaw, G., Jarosik, N., Kogut, A., Limon, M., Meyer, S. S., Page, L., Tucker, G. S., Weiland, J. L., Wollack, E., & Wright, E. L. 2003, *ApJS*, 148, 175
- Springel, V., Di Matteo, T., & Hernquist, L. 2005, *ApJ*, 620, L79
- Steidel, C. C., Adelberger, K. L., Shapley, A. E., Erb, D. K., Reddy, N. A., & Pettini, M. 2005, *ApJ*, 626, 44
- Steidel, C. C., Adelberger, K. L., Shapley, A. E., Pettini, M., Dickinson, M., & Giavalisco, M. 2003, *ApJ*, 592, 728
- Steidel, C. C., Shapley, A. E., Pettini, M., Adelberger, K. L., Erb, D. K., Reddy, N. A., & Hunt, M. P. 2004, *ApJ*, 604, 534
- Swinbank, A. M., Smail, I., Chapman, S. C., Blain, A. W., Ivison, R. J., & Keel, W. C. 2004, *ApJ*, 617, 64
- Tremaine, S., Gebhardt, K., Bender, R., Bower, G., Dressler, A., Faber, S. M., Filippenko, A. V., Green, R., Grillmair, C., Ho, L. C., Kormendy, J., Lauer, T. R., Magorrian, J., Pinkney, J., & Richstone, D. 2002, *ApJ*, 574, 740
- Tremonti, C. A., Heckman, T. M., Kauffmann, G., Brinchmann, J., Charlot, S., White, S. D. M., Seibert, M., Peng, E. W., Schlegel, D. J., Uomoto, A., Fukugita, M., & Brinkmann, J. 2004, *ApJ*, 613, 898
- van Dokkum, P. G., Franx, M., Förster Schreiber, N. M., Illingworth, G. D., Daddi, E., Knudsen, K. K., Labbé, I., Moorwood, A., Rix, H., Röttgering, H., Rudnick, G., Trujillo, I., van der Werf, P., van der Wel, A., van Starckenburg, L., & Wuyts, S. 2004, *ApJ*, 611, 703
- Wilson, J. C., Eikenberry, S. S., Henderson, C. P., Hayward, T. L., Carson, J. C., Pirger, B., Barry, D. J., Brandl, B. R., Houck, J. R., Fitzgerald, G. J., & Stolberg, T. M. 2003, in *Instrument Design and Performance for Optical/Infrared Ground-based Telescopes*. Edited by Iye, Masanori; Moorwood, Alan F. M. *Proceedings of the SPIE*, Volume 4841, pp. 451-458 (2003), 451-458

Yan, H., Dickinson, M., Eisenhardt, P. R. M., Ferguson, H. C.,
 Grogin, N. A., Paolillo, M., Chary, R.-R., Casertano, S., Stern,
 D., Reach, W. T., Moustakas, L. A., & Fall, S. M. 2004, ApJ,
 616, 63

TABLE 1
 GALAXIES OBSERVED

Object	R.A.	Dec.	$z_{H\alpha}$	\mathcal{R}^a	$G - \mathcal{R}^a$	$U_n - G^a$	K_s^b	$J - K_s^b$	Exposure time (s)
CDFb-BN88 ^c	00:53:52.87	12:23:51.25	2.2615	23.14	0.29	0.68	12 × 720
HDF-BX1055	12:35:59.59	62:13:07.50	2.4899	24.09	0.24	0.81	2 × 900
HDF-BX1084	12:36:13.57	62:12:21.48	2.4403	23.24	0.26	0.72	5 × 900
HDF-BX1085	12:36:13.33	62:12:16.31	2.2407	24.50	0.33	0.87	5 × 900
HDF-BX1086	12:36:13.41	62:12:18.84	2.4435	24.64	0.41	1.09	5 × 900
HDF-BX1277	12:37:18.59	62:09:55.54	2.2713	23.87	0.14	0.61	21.26	0.73	3 × 900
HDF-BX1303	12:37:11.20	62:11:18.67	2.3003	24.72	0.11	0.81	21.03	2.31	2 × 900
HDF-BX1311	12:36:30.54	62:16:26.12	2.4843	23.29	0.21	0.81	20.48	1.56	4 × 900
HDF-BX1322	12:37:06.54	62:12:24.94	2.4443	23.72	0.31	0.57	20.95	2.16	6 × 900
HDF-BX1332	12:37:17.13	62:11:39.95	2.2136	23.64	0.32	0.92	20.68	1.77	3 × 900
HDF-BX1368	12:36:48.24	62:15:56.24	2.4407	23.79	0.30	0.96	20.63	1.81	4 × 900
HDF-BX1376	12:36:52.96	62:15:45.55	2.4294	24.48	0.01	0.70	22.13	1.02	4 × 900
HDF-BX1388	12:36:44.84	62:17:15.84	2.0317	24.55	0.27	0.99	19.95	1.78	2 × 900
HDF-BX1397	12:37:04.12	62:15:09.84	2.1328	24.12	0.14	0.76	20.87	1.08	3 × 900
HDF-BX1409	12:36:47.41	62:17:28.70	2.2452	24.66	0.49	1.17	20.07	2.31	2 × 900
HDF-BX1439	12:36:53.66	62:17:24.27	2.1865	23.90	0.26	0.79	19.72	2.16	4 × 900
HDF-BX1479	12:37:15.42	62:16:03.88	2.3745	24.39	0.16	0.79	21.30	1.57	5 × 900
HDF-BX1564	12:37:23.47	62:17:20.02	2.2225	23.28	0.27	1.01	19.62	1.69	2 × 900
HDF-BX1567	12:37:23.17	62:17:23.89	2.2256	23.50	0.18	1.05	20.18	1.23	2 × 900
HDF-BX305	12:36:37.13	62:16:28.36	2.4839	24.28	0.79	1.30	20.14	2.59	4 × 900
HDF-BMZ1156	12:37:04.34	62:14:46.28	2.2151	24.62	-0.01	-0.21	20.33	1.71	4 × 900
Q0201-B13 ^c	02:03:49.25	11:36:10.58	2.1663	23.34	0.02	0.69	16 × 720
Q1307-BM1163	13:08:18.04	29:23:19.34	1.4105	21.66	0.20	0.35	2 × 900
Q1623-BX151	16:25:29.61	26:53:45.01	2.4393	24.60	0.14	0.88	2 × 900
Q1623-BX214	16:25:33.67	26:53:53.52	2.4700	24.06	0.39	1.12	4 × 900
Q1623-BX215	16:25:33.80	26:53:50.66	2.1814	24.45	0.26	0.53	4 × 900
Q1623-BX252	16:25:36.96	26:45:54.86	2.3367	25.06	0.07	0.55	3 × 900
Q1623-BX274	16:25:38.20	26:45:57.14	2.4100	23.23	0.25	0.89	3 × 900
Q1623-BX344	16:25:43.93	26:43:41.98	2.4224	24.42	0.39	1.25	2 × 900
Q1623-BX366	16:25:45.09	26:43:46.95	2.4204	23.84	0.41	1.03	2 × 900
Q1623-BX376	16:25:45.59	26:46:49.26	2.4085	23.31	0.24	0.75	20.84	1.61	4 × 900
Q1623-BX428	16:25:48.41	26:47:40.20	2.0538	23.95	0.13	1.06	20.72	1.02	4 × 900
Q1623-BX429	16:25:48.65	26:45:14.47	2.0160	23.63	0.12	0.56	20.94	1.46	2 × 900
Q1623-BX432	16:25:48.73	26:46:47.28	2.1817	24.58	0.10	0.53	21.48	1.76	4 × 900
Q1623-BX447	16:25:50.37	26:47:14.28	2.1481	24.48	0.17	1.14	20.55	1.66	3 × 900
Q1623-BX449	16:25:50.53	26:46:59.97	2.4188	24.86	0.20	0.61	21.35	1.88	3 × 900
Q1623-BX452	16:25:51.00	26:44:20.00	2.0595	24.73	0.20	0.90	20.56	2.05	3 × 900
Q1623-BX453	16:25:50.84	26:49:31.40	2.1816	23.38	0.48	0.99	19.76	1.65	3 × 900
Q1623-BX455	16:25:51.66	26:46:54.88	2.4074	24.80	0.35	0.87	21.56	1.83	2 × 900
Q1623-BX458	16:25:51.58	26:46:21.39	2.4194	23.41	0.28	0.85	20.52	1.23	4 × 900
Q1623-BX472	16:25:52.87	26:46:39.63	2.1142	24.58	0.16	0.91	22.80	1.91	4 × 900
Q1623-BX502	16:25:54.38	26:44:09.25	2.1558	24.35	0.22	0.50	22.04	0.99	3 × 900
Q1623-BX511	16:25:56.11	26:44:44.57	2.2421	25.37	0.42	1.05	21.78	...	4 × 900
Q1623-BX513	16:25:55.86	26:46:50.30	2.2473	23.25	0.26	0.68	20.21	1.83	2 × 900
Q1623-BX516	16:25:56.27	26:44:08.19	2.4236	23.94	0.30	0.82	20.41	2.29	3 × 900
Q1623-BX522	16:25:55.76	26:44:53.28	2.4757	24.50	0.31	1.19	20.75	2.03	4 × 900
Q1623-BX528	16:25:56.44	26:50:15.44	2.2682	23.56	0.25	0.71	19.75	1.79	4 × 900
Q1623-BX543	16:25:57.70	26:50:08.59	2.5211	23.11	0.44	0.96	20.54	1.31	4 × 900
Q1623-BX586	16:26:01.52	26:45:41.58	2.1045	24.58	0.32	0.87	20.84	1.79	4 × 900
Q1623-BX599	16:26:02.54	26:45:31.90	2.3304	23.44	0.22	0.80	19.93	2.09	4 × 900
Q1623-BX663	16:26:04.58	26:48:00.20	2.4333	24.14	0.24	1.02	19.92	2.59	3 × 900
Q1623-MD107	16:25:53.87	26:45:15.46	2.5373	25.35	0.12	1.43	22.43	1.72	4 × 900
Q1623-MD66	16:25:40.39	26:50:08.88	2.1075	23.95	0.37	1.40	20.15	1.74	3 × 900
Q1700-BX490	17:01:14.83	64:09:51.69	2.3960	22.88	0.36	0.92	19.99	1.54	3 × 900
Q1700-BX505	17:00:48.22	64:10:05.86	2.3089	25.17	0.45	1.28	20.85	2.17	4 × 900
Q1700-BX523	17:00:41.71	64:10:14.88	2.4756	24.51	0.46	1.28	20.93	1.86	4 × 900
Q1700-BX530	17:00:36.86	64:10:17.38	1.9429	23.05	0.21	0.69	19.92	1.23	4 × 900
Q1700-BX536	17:01:08.94	64:10:24.95	1.9780	23.00	0.21	0.79	19.71	1.31	4 × 900
Q1700-BX561	17:01:04.18	64:10:43.83	2.4332	24.65	0.19	1.04	19.87	2.43	2 × 900
Q1700-BX581	17:01:02.73	64:10:51.30	2.4022	23.87	0.28	0.62	20.79	1.94	2 × 900
Q1700-BX681	17:01:33.76	64:12:04.28	1.7396	22.04	0.19	0.40	19.18	1.27	4 × 900
Q1700-BX691	17:01:06.00	64:12:10.27	2.1895	25.33	0.22	0.66	20.68	1.82	4 × 900
Q1700-BX717	17:00:56.99	64:12:23.76	2.4353	24.78	0.20	0.61	21.89	1.49	4 × 900
Q1700-BX759	17:00:59.55	64:12:55.45	2.4213	24.43	0.36	1.29	21.23	1.35	2 × 900
Q1700-BX794	17:00:47.30	64:13:18.70	2.2473	23.60	0.35	0.58	20.53	1.37	3 × 900
Q1700-BX917	17:01:16.11	64:14:19.80	2.3069	24.43	0.28	0.95	20.03	1.95	3 × 900
Q1700-MD103	17:01:00.21	64:11:55.58	2.3148	24.23	0.46	1.49	19.94	1.96	900 + 600
Q1700-MD109	17:01:04.48	64:12:09.29	2.2942	25.46	0.26	1.44	21.77	1.75	4 × 900
Q1700-MD154	17:01:38.39	64:14:57.37	2.6291	23.23	0.73	1.91	19.68	2.08	3 × 900

TABLE 1 — *Continued*

Object	R.A.	Dec.	$z_{\text{H}\alpha}$	\mathcal{R}^a	$G - \mathcal{R}^a$	$U_n - G^a$	K_s^b	$J - K_s^b$	Exposure time (s)
Q1700-MD174	17:00:54.54	64:16:24.76	2.3423	24.56	0.32	1.50	19.90	...	4×900
Q1700-MD69	17:00:47.62	64:09:44.78	2.2883	24.85	0.37	1.50	20.05	2.60	4×900
Q1700-MD94	17:00:42.02	64:11:24.22	2.3362	24.72	0.94	2.06	19.65	2.46	3×900
Q2343-BM133	23:46:16.18	12:48:09.31	1.4774	22.59	0.00	0.19	20.50	0.66	3×900
Q2343-BM181	23:46:27.03	12:49:19.65	1.4951	24.77	0.12	0.29	4×900
Q2343-BX163	23:46:04.78	12:45:37.78	2.1213	24.07	-0.01	0.71	21.38	0.97	4×900
Q2343-BX169	23:46:05.03	12:45:40.77	2.2094	23.11	0.19	0.72	20.75	1.05	4×900
Q2343-BX182	23:46:18.04	12:45:51.11	2.2879	23.74	0.14	0.56	21.60	0.92	4×900
Q2343-BX236	23:46:18.71	12:46:15.97	2.4348	24.28	0.14	0.71	21.25	1.60	3×900
Q2343-BX336	23:46:29.53	12:47:04.76	2.5439	23.91	0.40	1.15	20.80	1.75	4×900
Q2343-BX341	23:46:23.24	12:47:07.97	2.5749	24.21	0.38	0.89	21.40	2.07	3×900
Q2343-BX378	23:46:33.90	12:47:26.20	2.0441	24.80	0.26	0.55	21.90	1.30	4×900
Q2343-BX389	23:46:28.90	12:47:33.55	2.1716	24.85	0.28	1.26	20.18	2.74	3×900
Q2343-BX390	23:46:24.72	12:47:33.80	2.2313	24.36	0.24	0.79	21.29	1.73	4×900
Q2343-BX391	23:46:28.07	12:47:31.82	2.1740	24.51	0.25	1.01	21.93	1.35	3×900
Q2343-BX418	23:46:18.57	12:47:47.38	2.3052	23.99	-0.05	0.37	21.88	1.76	5×900
Q2343-BX429	23:46:25.25	12:47:51.20	2.1751	25.12	0.30	0.85	21.88	1.97	4×900
Q2343-BX435	23:46:26.36	12:47:55.06	2.1119	24.23	0.38	1.03	20.38	1.75	4×900
Q2343-BX436	23:46:09.06	12:47:56.00	2.3277	23.07	0.12	0.47	21.04	0.73	4×900
Q2343-BX442	23:46:19.36	12:47:59.69	2.1760	24.48	0.40	1.14	19.85	2.36	5×900
Q2343-BX461	23:46:32.96	12:48:08.15	2.5662	24.40	0.44	0.90	21.67	1.99	4×900
Q2343-BX474	23:46:32.88	12:48:14.08	2.2257	24.42	0.31	1.15	20.56	1.73	4×900
Q2343-BX480	23:46:21.90	12:48:15.61	2.2313	23.77	0.29	1.03	20.44	1.92	4×900
Q2343-BX493	23:46:14.46	12:48:21.64	2.3396	23.63	0.28	0.78	21.65	0.75	2×900
Q2343-BX513	23:46:11.13	12:48:32.14	2.1092 ^d	23.93	0.20	0.41	20.10	1.87	4×900
Q2343-BX529	23:46:09.72	12:48:40.33	2.1129	24.42	0.20	0.91	21.41	1.52	2×900
Q2343-BX537	23:46:25.55	12:48:44.54	2.3396	24.44	0.23	0.72	21.43	1.65	4×900
Q2343-BX587	23:46:29.18	12:49:03.34	2.2430	23.47	0.32	1.12	20.12	1.82	3×900
Q2343-BX599	23:46:13.85	12:49:11.31	2.0116	23.50	0.10	0.81	20.40	1.19	4×900
Q2343-BX601	23:46:20.40	12:49:12.91	2.3769	23.48	0.22	0.75	20.55	1.50	4×900
Q2343-BX610	23:46:09.43	12:49:19.21	2.2094	23.58	0.34	0.75	19.21	2.24	4×900
Q2343-BX660	23:46:29.43	12:49:45.54	2.1735	24.36	-0.09	0.45	20.98	2.26	2×900
Q2343-MD59	23:46:26.90	12:47:39.87	2.0116	24.99	0.20	1.47	20.14	2.59	4×900
Q2343-MD62	23:46:27.23	12:47:43.48	2.1752	25.29	0.21	1.23	21.45	2.23	4×900
Q2343-MD80	23:46:10.79	12:48:33.24	2.0138	24.81	0.09	1.33	21.38	1.15	4×900
Q2346-BX120	23:48:26.30	00:20:33.16	2.2664	25.08	0.02	0.91	4×900
Q2346-BX220	23:48:46.10	00:22:20.95	1.9677	23.57	0.29	0.90	20.82	...	4×900
Q2346-BX244	23:48:09.61	00:22:36.18	1.6465	24.54	0.41	1.16	4×900
Q2346-BX404	23:48:21.40	00:24:43.07	2.0282	23.39	0.18	0.41	20.05	...	5×900
Q2346-BX405	23:48:21.22	00:24:45.46	2.0300	23.36	0.08	0.60	20.27	...	5×900
Q2346-BX416	23:48:18.21	00:24:55.30	2.2404	23.49	0.40	0.75	20.30	...	3×900
Q2346-BX482	23:48:12.97	00:25:46.34	2.2569	23.32	0.22	0.90	4×900
SSA22a-MD41 ^c	22:17:39.97	00:17:11.04	2.1713	23.31	0.19	1.31	15×720
West-BM115	14:17:37.57	52:27:05.42	1.6065	23.41	0.28	0.36	10×900
West-BX600	14:17:15.55	52:36:15.64	2.1607	23.94	0.10	0.46	5×900

^a U_n , G and \mathcal{R} magnitudes are AB.

^b J and K_s magnitudes are Vega.

^c Observed with the ISAAC spectrograph on the VLT; previously discussed by Erb et al. (2003).

^d Q2343-BX513 was observed a second time with a different position angle, and yielded an $\text{H}\alpha$ redshift $z_{\text{H}\alpha} = 2.1079$.

TABLE 2
NEAR-IR IMAGING

Field	Band	Exposure time (hrs)	Depth ^a
GOODS-N	J	13.0	24.1
	K_s	10.3	22.6
Q1623	J	9.8	23.8
	K_s	11.2	22.3
Q1700	J	10.7	24.0
	K_s	11.0	22.2
Q2343	J	10.7	24.0
	K_s	12.1	22.3
Q2346	K_s	2.6	21.2

^a Approximate 3σ image depth, in Vega magnitudes.

TABLE 3
RESULTS OF SED FITTING

Object	τ (Myr)	$E(B - V)^a$	Age ^b (Myr)	SFR ^c ($M_{\odot} \text{ yr}^{-1}$)	M_{\star}^d ($10^{10} M_{\odot}$)
HDF-BMZ1156	500	0.000	1900	4	9.6
HDF-BX1277	const	0.095	321	15	0.5
HDF-BX1303	const	0.100	1139	7	0.8
HDF-BX1311	const	0.105	255	34	0.9
HDF-BX1322	const	0.085	360	19	0.7
HDF-BX1332	const	0.290	15	159	0.2
HDF-BX1368	const	0.160	404	37	1.5
HDF-BX1376	const	0.070	227	9	0.2
HDF-BX1388	const	0.265	3000	23	7.0
HDF-BX1397	const	0.150	1015	17	1.7
HDF-BX1409	const	0.290	1015	27	2.7
HDF-BX1439	const	0.175	2100	21	4.5
HDF-BX1479	const	0.110	806	13	1.0
HDF-BX1564	100	0.065	360	9	3.3
HDF-BX1567	50	0.050	227	5	2.3
HDF-BX305	const	0.285	571	53	3.0
Q1623-BX376	const	0.175	64	80	0.5
Q1623-BX428	50	0.000	255	1	1.1
Q1623-BX429	const	0.120	227	23	0.5
Q1623-BX432	const	0.060	1278	6	0.8
Q1623-BX447	500	0.050	1434	5	4.4
Q1623-BX449	const	0.110	2600	9	2.4
Q1623-BX452	const	0.195	3000	14	4.3
Q1623-BX453	const	0.275	454	107	4.9
Q1623-BX455	const	0.265	15	58	0.09
Q1623-BX458	const	0.165	571	55	3.1
Q1623-BX472	const	0.130	3000	11	3.2
Q1623-BX502	const	0.220	6	72	0.04
Q1623-BX511	const	0.235	571	13	0.8
Q1623-BX513	const	0.145	454	46	2.1
Q1623-BX516	const	0.145	1800	28	5.1
Q1623-BX522	const	0.180	2600	24	6.2
Q1623-BX528	const	0.175	2750	44	12.2
Q1623-BX543	const	0.305	8	528	0.4
Q1623-BX586	const	0.195	1434	17	2.5
Q1623-BX599	const	0.125	1900	35	6.7
Q1623-BX663	1000	0.135	2000	21	13.2
Q1623-MD107	const	0.060	1015	4	0.4
Q1623-MD66	const	0.235	905	43	3.9
Q1700-BX490	const	0.285	10	448	0.4
Q1700-BX505	const	0.270	1800	20	3.6
Q1700-BX523	const	0.260	255	42	1.1
Q1700-BX530	50	0.045	203	6	1.8
Q1700-BX536	50	0.115	180	15	2.8
Q1700-BX561	500	0.130	1609	10	11.5
Q1700-BX581	const	0.215	35	70	0.2
Q1700-BX681	const	0.315	10	628	0.6
Q1700-BX691	1000	0.125	2750	5	7.6
Q1700-BX717	const	0.090	509	8	0.4
Q1700-BX759	const	0.230	640	37	2.4
Q1700-BX794	const	0.130	454	25	1.1
Q1700-BX917	200	0.040	806	4	4.0
Q1700-MD103	const	0.305	1015	65	6.6
Q1700-MD109	const	0.175	2200	8	1.7
Q1700-MD154	const	0.335	128	347	4.4
Q1700-MD174	1000	0.195	2400	24	23.6
Q1700-MD69	2000	0.275	2750	31	18.6
Q1700-MD94	const	0.500	719	213	15.3
Q2343-BM133	const	0.115	143	35	0.5
Q2343-BX163	const	0.050	1434	9	1.3
Q2343-BX169	const	0.125	203	46	0.9
Q2343-BX182	const	0.100	180	23	0.4
Q2343-BX236	const	0.085	1680	13	2.1
Q2343-BX336	const	0.210	321	58	1.9
Q2343-BX341	const	0.210	102	50	0.5
Q2343-BX378	const	0.165	255	11	0.3
Q2343-BX389	const	0.250	2750	22	6.1
Q2343-BX390	const	0.150	404	17	0.7
Q2343-BX391	const	0.195	64	25	0.2
Q2343-BX418	const	0.035	81	12	0.1
Q2343-BX429	const	0.185	321	12	0.4
Q2343-BX435	const	0.225	1434	30	4.4
Q2343-BX436	const	0.070	321	33	1.1
Q2343-BX442	2000	0.225	2750	25	14.7

TABLE 3 — *Continued*

Object	τ (Myr)	$E(B-V)^a$	Age ^b (Myr)	SFR ^c ($M_\odot \text{ yr}^{-1}$)	M_\star^d ($10^{10} M_\odot$)
Q2343-BX461	const	0.250	15	86	0.1
Q2343-BX474	const	0.215	2750	26	7.2
Q2343-BX480	const	0.165	905	33	3.0
Q2343-BX493	const	0.255	6	220	0.1
Q2343-BX513	const	0.135	3000	20	5.9
Q2343-BX529	const	0.145	404	14	0.6
Q2343-BX537	const	0.130	571	15	0.8
Q2343-BX587	const	0.180	719	49	3.5
Q2343-BX599	const	0.100	1609	21	3.3
Q2343-BX601	const	0.125	640	36	2.3
Q2343-BX610	1000	0.155	2100	32	23.2
Q2343-BX660	const	0.010	2750	5	1.4
Q2343-MD59	2000	0.200	3000	11	7.6
Q2343-MD62	const	0.150	2750	7	1.9
Q2343-MD80	50	0.020	255	1	0.6
Q2346-BX220	50	0.055	227	4	1.7
Q2346-BX404	const	0.095	1800	22	4.0
Q2346-BX405	100	0.010	321	7	1.6
Q2346-BX416	const	0.195	454	55	2.5

^a Typical uncertainty $\langle \sigma_{E(B-V)}/E(B-V) \rangle = 0.7$.

^b Typical uncertainty $\langle \sigma_{\text{Age}}/\text{Age} \rangle = 0.5$.

^c Typical uncertainty $\langle \sigma_{\text{SFR}}/\text{SFR} \rangle = 0.6$.

^d Typical uncertainty $\langle \sigma_{M_\star}/M_\star \rangle = 0.4$.

TABLE 4
KINEMATICS

Object	$z_{\text{H}\alpha}$	z_{abs}^a	$z_{\text{Ly}\alpha}^b$	$F_{\text{H}\alpha}^c$	$r_{\text{H}\alpha}^d$ (kpc)	σ^e (km s^{-1})	v_c^f (km s^{-1})	M_{dyn}^g ($10^{10} M_\odot$)	M_\star^h ($10^{10} M_\odot$)
CDFb-BN88	2.2615	2.6 ± 0.2	7.4	96^{+20}_{-20}	...	5.3	...
HDF-BX1055	2.4899	2.4865	2.4959	2.6 ± 0.6	3.8	< 59	...	< 1.0	...
HDF-BX1084	2.4403	2.4392	...	7.3 ± 0.2	4.8	102^{+6}_{-6}	...	5.1	...
HDF-BX1085	2.2407	2.2381	...	1.1 ± 0.1	2.4
HDF-BX1086	2.4435	1.8 ± 0.2	< 1.9	95^{+20}_{-20}	...	< 1.6	...
HDF-BX1277	2.2713	2.2686	...	5.3 ± 0.2	5.0	63^{+9}_{-10}	...	1.3	0.5
HDF-BX1303	2.3003	2.3024	2.3051	2.6 ± 0.5	3.4	0.8
HDF-BX1311	2.4843	2.4804	2.4890	8.0 ± 0.4	5.5	88^{+9}_{-9}	...	3.2	0.9
HDF-BX1322	2.4443	2.4401	2.4491	2.0 ± 0.2	4.6	< 47	...	< 1.1	0.7
HDF-BX1332	2.2136	2.2113	...	4.4 ± 0.3	5.5	54^{+16}_{-20}	47 ± 14	1.2	0.2
HDF-BX1368	2.4407	2.4380	2.4455	8.8 ± 0.4	7.4	139^{+9}_{-9}	...	6.6	1.5
HDF-BX1376	2.4294	2.4266	2.4338	2.2 ± 0.2	2.9	96^{+22}_{-24}	...	2.2	0.2
HDF-BX1388	2.0317	2.0305	...	5.8 ± 0.5	7.9	140^{+21}_{-21}	...	11.7	7.0
HDF-BX1397	2.1328	2.1322	...	5.3 ± 0.5	8.6	125^{+22}_{-24}	109 ± 19	10.3	1.7
HDF-BX1409	2.2452	2.2433	...	8.5 ± 0.6	7.0	158^{+18}_{-18}	...	13.3	2.7
HDF-BX1439	2.1865	2.1854	2.1913	8.8 ± 0.3	8.2	120^{+8}_{-8}	...	8.6	4.5
HDF-BX1479	2.3745	2.3726	2.3823	2.5 ± 0.2	4.3	46^{+18}_{-21}	...	0.9	1.0
HDF-BX1564	2.2225	2.2219	...	8.6 ± 0.7	15.4	99^{+16}_{-18}	...	11.7	3.3
HDF-BX1567	2.2256	2.2257	...	4.0 ± 0.6	2.6	< 62	...	< 1.8	2.3
HDF-BX305	2.4839	2.4825	...	4.2 ± 0.4	3.8	140^{+22}_{-24}	...	5.6	3.0
HDF-BMZ1156 ⁱ	2.2151	5.4 ± 0.4	< 1.9	196^{+24}_{-26}	...	< 7.1	9.6
Q0201-B13	2.1663	2.4 ± 0.1	7.4	62^{+10}_{-10}	...	2.2	...
Q1307-BM1163	1.4105	1.4080	...	28.7 ± 1.2	6.7	125^{+8}_{-8}	...	8.2	...
Q1623-BX151 ⁱ	2.4393	3.5 ± 0.6	8.4	98^{+36}_{-40}	...	6.3	...
Q1623-BX214	2.4700	2.4674	...	5.3 ± 0.4	4.1	55^{+14}_{-15}	...	1.0	...
Q1623-BX215	2.1814	2.1819	...	4.8 ± 0.3	5.0	70^{+15}_{-16}	...	2.0	...
Q1623-BX252	2.3367	1.1 ± 0.3	< 1.9
Q1623-BX274	2.4100	2.4081	2.4130	9.5 ± 0.3	4.8	121^{+9}_{-9}	...	5.5	...
Q1623-BX344	2.4224	17.1 ± 0.8	4.1	92^{+9}_{-10}	...	2.7	...
Q1623-BX366	2.4204	2.4169	...	7.8 ± 1.5	8.4	103^{+39}_{-44}	...	7.0	...
Q1623-BX376	2.4085	2.4061	2.4153	5.3 ± 0.7	7.0	261^{+54}_{-54}	...	36.6	0.5
Q1623-BX428	2.0538	2.0514	2.0594	2.7 ± 0.5	1.4	1.1
Q1623-BX429	2.0160	2.0142	...	5.1 ± 0.5	6.7	57^{+22}_{-27}	...	1.7	0.5
Q1623-BX432	2.1817	5.4 ± 0.3	4.6	54^{+15}_{-16}	...	1.0	0.8
Q1623-BX447	2.1481	2.1478	...	5.6 ± 0.3	5.3	174^{+15}_{-15}	160 ± 22	12.5	4.4

TABLE 4 — *Continued*

Object	$z_{\text{H}\alpha}$	$z_{\text{abs}}^{\text{a}}$	$z_{\text{Ly}\alpha}^{\text{b}}$	$F_{\text{H}\alpha}^{\text{c}}$	$r_{\text{H}\alpha}^{\text{d}}$ (kpc)	σ^{e} (km s $^{-1}$)	v_{c}^{f} (km s $^{-1}$)	$M_{\text{dyn}}^{\text{g}}$ ($10^{10} M_{\odot}$)	M_{\star}^{h} ($10^{10} M_{\odot}$)
Q1623-BX449	2.4188	3.5 ± 0.9	< 1.9	< 72	...	< 2.5	2.4
Q1623-BX452	2.0595	2.0595	...	4.4 ± 0.4	9.6	129^{+20}_{-20}	...	12.9	4.3
Q1623-BX453	2.1816	2.1724	2.1838	13.8 ± 0.2	4.1	61^{+4}_{-4}	...	1.2	4.9
Q1623-BX455	2.4074	2.4066	...	18.8 ± 1.1	5.0	187^{+15}_{-15}	...	13.6	0.09
Q1623-BX458	2.4194	2.4174	...	4.3 ± 0.5	8.4	160^{+10}_{-27}	116 ± 18	16.8	3.1
Q1623-BX472	2.1142	2.1144	...	3.9 ± 0.2	6.0	110^{+10}_{-10}	110 ± 12	5.7	3.2
Q1623-BX502	2.1558	2.1549	2.1600	13.2 ± 0.4	6.2	75^{+8}_{-8}	...	2.7	0.04
Q1623-BX511	2.2421	3.4 ± 0.3	6.2	152^{+34}_{-36}	80 ± 18	11.3	0.8
Q1623-BX513	2.2473	2.2469	2.2525	3.3 ± 0.3	3.4	2.1
Q1623-BX516	2.4236	2.4217	...	5.2 ± 1.0	2.6	114^{+15}_{-16}	...	2.7	5.1
Q1623-BX522	2.4757	2.4742	...	2.8 ± 0.3	6.2	< 46	...	< 1.0	6.2
Q1623-BX528	2.2682	2.2683	...	7.7 ± 0.4	7.9	142^{+14}_{-14}	76 ± 12	12.0	12.2
Q1623-BX543	2.5211	2.5196	...	8.6 ± 0.7	7.4	148^{+24}_{-26}	...	12.6	0.4
Q1623-BX586	2.1045	5.1 ± 0.4	5.3	124^{+18}_{-20}	...	6.2	2.5
Q1623-BX599	2.3304	2.3289	2.3402	18.1 ± 0.4	5.8	162^{+8}_{-8}	...	11.6	6.7
Q1623-BX663 ⁱ	2.4333	2.4296	2.4353	8.2 ± 0.3	7.0	132^{+12}_{-14}	...	9.3	13.2
Q1623-MD107	2.5373	3.7 ± 0.4	3.6	< 43	...	< 0.9	0.4
Q1623-MD66	2.1075	2.1057	...	19.7 ± 0.3	5.3	120^{+4}_{-4}	...	5.9	3.9
Q1700-BX490	2.3960	2.3969	2.4043	17.7 ± 0.6	5.5	110^{+9}_{-9}	...	5.1	0.4
Q1700-BX505	2.3089	3.6 ± 0.3	7.4	120^{+20}_{-21}	...	8.3	3.6
Q1700-BX523	2.4756	4.7 ± 0.5	7.7	130^{+26}_{-26}	...	9.9	1.1
Q1700-BX530	1.9429	1.9411	...	12.2 ± 0.7	6.2	< 37	...	< 0.6	1.8
Q1700-BX536	1.9780	11.3 ± 0.7	7.9	89^{+14}_{-15}	...	4.7	2.8
Q1700-BX561	2.4332	2.4277	...	1.9 ± 0.6	< 1.9	11.5
Q1700-BX581	2.4022	2.3984	...	4.0 ± 0.7	4.3	0.2
Q1700-BX681	1.7396	1.7398	1.7467	6.3 ± 0.2	8.6	0.6
Q1700-BX691	2.1895	7.7 ± 0.3	6.7	170^{+14}_{-14}	220 ± 14	15.0	7.6
Q1700-BX717	2.4353	...	2.4376	3.8 ± 0.4	4.8	< 47	...	< 1.1	0.4
Q1700-BX759	2.4213	1.3 ± 0.5	2.4	2.4
Q1700-BX794	2.2473	6.8 ± 0.4	4.8	80^{+14}_{-14}	...	2.4	1.1
Q1700-BX917	2.3069	2.3027	...	7.4 ± 0.5	10.6	99^{+12}_{-14}	...	8.2	4.0
Q1700-MD69	2.2883	2.288	...	8.2 ± 0.9	9.4	155^{+15}_{-16}	...	17.2	18.6
Q1700-MD94 ⁱ	2.3362	2.8 ± 0.3	9.6	730^{+82}_{-82}	...	382	15.3
Q1700-MD103	2.3148	4.1 ± 0.8	8.4	75^{+21}_{-24}	100 ± 19	3.7	6.6
Q1700-MD109	2.2942	8.9 ± 0.7	4.1	93^{+24}_{-26}	...	2.7	1.7
Q1700-MD154	2.6291	7.5 ± 0.5	8.2	57^{+34}_{-50}	...	2.1	4.4
Q1700-MD174 ⁱ	2.3423	12.9 ± 1.4	3.6	444^{+50}_{-50}	...	56.5	23.6
Q2343-BM133	1.4774	1.4769	...	28.7 ± 0.8	7.7	55^{+6}_{-6}	...	1.8	0.5
Q2343-BM181	1.4951	1.4952	...	3.4 ± 0.5	7.7	39^{+17}_{-30}	45 ± 18	1.0	...
Q2343-BX163	2.1213	2.2 ± 0.4	4.1	1.3
Q2343-BX169	2.2094	2.2105	2.2173	4.7 ± 0.3	3.1	0.9
Q2343-BX182	2.2879	2.2857	2.2909	2.4 ± 0.3	2.6	0.4
Q2343-BX236	2.4348	2.4304	2.4372	3.1 ± 0.6	4.8	148^{+40}_{-42}	...	8.2	2.1
Q2343-BX336	2.5439	2.5448	2.5516	4.3 ± 0.6	5.0	140^{+33}_{-34}	...	7.6	1.9
Q2343-BX341	2.5749	2.5715	...	4.0 ± 0.6	2.4	0.5
Q2343-BX378	2.0441	4.5 ± 1.0	7.4	0.3
Q2343-BX389	2.1716	2.1722	...	12.0 ± 0.4	10.1	111^{+8}_{-8}	71 ± 10	9.6	6.1
Q2343-BX390	2.2313	2.2290	...	4.9 ± 0.5	10.8	78^{+21}_{-24}	...	5.1	0.7
Q2343-BX391	2.1740	2.1714	...	4.2 ± 0.2	6.0	0.2
Q2343-BX418	2.3052	2.3030	2.3084	8.0 ± 0.2	3.6	66^{+6}_{-6}	...	1.2	0.1
Q2343-BX429	2.1751	4.8 ± 0.3	9.4	51^{+16}_{-20}	...	1.9	0.4
Q2343-BX435	2.1119	2.1088	2.1153	8.1 ± 0.4	8.9	60^{+12}_{-14}	...	2.4	4.4
Q2343-BX436	2.3277	2.3253	2.3315	7.2 ± 0.4	9.1	63^{+10}_{-12}	...	2.8	1.1
Q2343-BX442	2.1760	7.1 ± 0.3	10.6	132^{+9}_{-9}	...	13.5	14.7
Q2343-BX461	2.5662	2.5649	2.5759	7.0 ± 0.7	7.7	139^{+22}_{-24}	...	11.5	0.1
Q2343-BX474	2.2257	2.2263	...	5.0 ± 0.3	7.0	84^{+12}_{-12}	...	3.8	7.2
Q2343-BX480	2.2313	2.2297	2.2352	3.0 ± 0.2	3.4	< 37	...	< 0.7	3.0
Q2343-BX493	2.3396	2.3375	2.3447	5.3 ± 0.9	6.5	155^{+39}_{-42}	...	12.2	0.1
Q2343-BX513 ^j	2.1092	2.1090	2.114	10.1 ± 0.4	4.1	150^{+9}_{-9}	...	7.0	5.9
Q2343-BX529	2.1129	2.1116	2.1190	3.5 ± 0.5	< 1.9	0.6
Q2343-BX537	2.3396	5.2 ± 0.3	5.3	0.8
Q2343-BX587	2.2430	2.2382	...	5.5 ± 0.4	7.7	94^{+14}_{-15}	...	5.2	3.5
Q2343-BX599	2.0116	2.0112	...	4.5 ± 0.4	7.2	77^{+21}_{-22}	...	3.3	3.3

TABLE 4 — *Continued*

Object	$z_{\text{H}\alpha}$	$z_{\text{abs}}^{\text{a}}$	$z_{\text{Ly}\alpha}^{\text{b}}$	$F_{\text{H}\alpha}^{\text{c}}$	$r_{\text{H}\alpha}^{\text{d}}$ (kpc)	σ^{e} (km s $^{-1}$)	v_{c}^{f} (km s $^{-1}$)	$M_{\text{dyn}}^{\text{g}}$ ($10^{10} M_{\odot}$)	M_{\star}^{h} ($10^{10} M_{\odot}$)
Q2343-BX601	2.3769	2.3745	2.3823	7.4 ± 0.4	5.3	105^{+12}_{-12}	...	4.5	2.3
Q2343-BX610	2.2094	2.2083	2.2129	8.1 ± 0.4	8.4	96^{+9}_{-10}	...	6.1	23.2
Q2343-BX660	2.1735	2.1709	2.1771	9.4 ± 0.4	6.2	< 40	...	< 0.8	1.4
Q2343-MD59	2.0116	2.0107	...	2.9 ± 0.4	5.5	7.6
Q2343-MD62	2.1752	2.1740	...	2.3 ± 0.3	6.7	79^{+27}_{-30}	...	3.3	1.9
Q2343-MD80	2.0138	2.0116	...	3.2 ± 0.3	2.6	74^{+16}_{-16}	...	1.1	0.6
Q2346-BX120	2.2664	5.3 ± 0.3	6.2	62^{+12}_{-12}	40 ± 10	1.9	...
Q2346-BX220	1.9677	1.9664	...	10.3 ± 0.6	6.5	143^{+14}_{-14}	...	10.4	1.7
Q2346-BX244	1.6465	1.6462	1.6516	5.4 ± 0.8	7.7	42^{+27}_{-42}	...	1.0	...
Q2346-BX404	2.0282	2.0270	2.0348	13.9 ± 0.3	3.6	102^{+3}_{-3}	...	3.0	4.0
Q2346-BX405	2.0300	2.0298	2.0358	14.0 ± 0.2	5.8	50^{+4}_{-4}	...	1.1	1.6
Q2346-BX416	2.2404	2.2407	...	12.1 ± 0.7	4.3	126^{+12}_{-14}	...	5.3	2.5
Q2346-BX482	2.2569	2.2575	...	11.2 ± 0.3	9.8	133^{+4}_{-4}	...	13.7	...
SSA22a-MD41	2.1713	7.9 ± 0.1	9.6	107^{+6}_{-6}	150 ± 16	8.2	...
West-BM115	1.6065	1.6060	...	5.9 ± 0.4	5.5	128^{+15}_{-15}	...	6.9	...
West-BX600	2.1607	6.3 ± 0.4	8.2	181^{+16}_{-16}	210 ± 13	21.5	...

^a Vacuum redshift of the UV interstellar absorption lines. We give a value only when the S/N of the spectrum is sufficient for a precise measurement.

^b Vacuum redshift of the Ly α emission line, when present.

^c Observed flux of H α emission line, in units of 10^{-17} erg s $^{-1}$ cm $^{-2}$.

^d Approximate spatial extent of the H α emission (FWHM), after subtraction of the seeing in quadrature.

^e Velocity dispersion of the H α emission line.

^f For tilted emission lines, the velocity shear $(v_{\text{max}} - v_{\text{min}})/2$, where v_{max} and v_{min} are with respect to the systemic redshift.

^g Dynamical mass $M_{\text{dyn}} = 3.4\sigma^2 r_{\text{H}\alpha}/G$.

^h Stellar mass, from SED modeling.

ⁱ AGN

^j Q2343-BX513 was observed twice with NIRSPEC, with position angles differing by 9° . The first observation yielded $z_{\text{H}\alpha} = 2.1079$ and $\sigma = 58$ km s $^{-1}$, and the second $z_{\text{H}\alpha} = 2.1092$ and $\sigma = 150$ km s $^{-1}$. It also has two Ly α emission redshifts, $z_{\text{Ly}\alpha} = 2.106$ and $z_{\text{Ly}\alpha} = 2.114$.